Fuel Cell Hybrid Vehicle Modeling in Modelica

Sara Sigfridsson

LUND
UNIVERSITY

Department of Automatic Control

MSc Thesis
TFRT-6052
ISSN 0280-5316

Department of Automatic Control
Lund University
Box 118
SE-221 00 LUND
Sweden

Printed in Sweden by Tryckeriet i E-huset
Lund 2018

Abstract

Exchanging classical combustion motors in cars for more environmentally friendly solutions is a hot topic worldwide and this has currently been taken to a new dimension by the release of the first hydrogen driven vehicles on the world market.

The objective of this master thesis has been to develop a Modelica model of an automotive hydrogen fuel cell system, which should be integrated in an already existing vehicle system template and be simulated in various drive cycle tests. The work was performed in the Modelica platform Dymola by means of its Fuel Cell and Vehicle Dynamics Libraries.

The model was constructed and parameterized according to available information of the commercial hydrogen driven car, Toyota Mirai.

The purpose of the developed system model was to monitor overall performance and efficiency during various dynamic drive cycles and operating conditions. The model should reproduce realistic output signals during simulation. It should also capture the effects of changes of a wide range of operation or boundary conditions, such as internal and external temperatures, operation pressure and variations in humidity in the stack system.

The developed stack system model contained controlled systems for air and fuel supply, an external humidifier and an advanced cooling system. The power consumption of the auxiliary device and the fuel cell and stack system efficiency could also be monitored. The power train system consisted of a rechargeable battery, a DC motor, two DC/DC converters and software to direct the current withdrawn from the stack according to the motor demands. The final fuel cell vehicle system model was validated and simulated in a set of established dynamic drive cycles.

The model was mimicking the Mirai well, although certain assumptions had been performed due to limited system information or reasonable simplifications.

Acknowledgements

I would like to thank my supervisors at Modelon, Lixiang Li and Håkan Runvik, for their support and helpfulness during my thesis work. I am grateful for Håkan's assistance with Dymola and patience with my questions, but also for the fruitful discussions within the field of physics. I also wish to thank Lixiang for his sharing of knowledge within fuel cells and thermodynamics, his always positive attitude and his structured supervision from the other side of the Atlantic Ocean.

I would also like to mention Kristian Soltesz, my supervisor at the department of Automatic Control at Lund University, for providing structure and contributing with good advice to my work. It has been appreciated.

Further, I thank the staff at Modelon for the pleasant time spent at their company.

Last, but not least, I would like to thank my family and close friends for their love and support during all of my education - you all know who you are and I would not have succeeded without you!

Acronyms

Abbreviations	
AC	Alternating Current
AFC	Alkaline Fuel Cell
BEV	Battery Electric Vehicle
CHP	Combined Heat and Power
DAE	Differential Algebraic Equation
DC	Direct Current
DMFC	Direct Methanol Fuel Cell
EPA	United States Environmental Protection Agency
FCEV	Fuel Cell Electric Vehicle
FCHV	Fuel Cell Hybrid Vehicle
FCL	Fuel Cell Library
FMI	Functional Mock-up Interface
ICE	Internal Combustion Engine
LHV	Lower Heat Value
MEA	Membrane Electrolyte Assembly
MCFC	Molten Carbonate Fuel Cell
PCU	Power Control Unit
PAFC	Phosphoric Acid Fuel Cell
PEM	Proton Exchange Membrane alt. Polymer Electrolyte Membrane
PEMFC	Proton Exchange Membrane Fuel Cell
RH	Relative Humidity
SOC	State of Charge
SOFC	Solid Oxide Fuel Cell
SVN	Subversion
VDL	Vehicle Dynamics Library

Contents

1

Introduction

As environmental and energy-related issues, such as air pollution and global warming, are becoming increasingly severe worldwide, hydrogen is successively gaining attention as a future alternative to traditional fossil fuels. The technology can be viewed as an extension of electrification of vehicles, which implies that the engine efficiency is far superior to the combustion motor and also that the emission during consumption is carbon dioxide neutral.

In this chapter, the purpose of this project and its scope will be clarified. The development of hydrogen driven vehicles and also fuel cells and their application within the car industry will be discussed to give a background of this thesis work. Additionally, the programming language to be used, Modelica, and the development environment, Dymola, will also be briefly described.

1.1 Purpose and Scope

The objective of this master thesis is to develop a Modelica model of an automotive hydrogen fuel cell system, which should be integrated in an already existing vehicle system template. The model should be simulated in various drive cycle tests provided from Modelon's Fuel Cell Hybrid Vehicle (FCHV) Library. The purpose of the developed model system is to monitor overall performance and efficiency during various dynamic drive cycles and operating conditions (not only ambient conditions, but also inner design criteria, such as stack temperature, membrane humidification and cooling system). Hence, the scientific objective of the model is to capture relevant physics in the fuel cell system and the drive-line and also to be able to predict the behavior of a corresponding vehicle.

From a market perspective, the model should be able to catch the interest of targeted customers within the vehicle industry, but also institutes and research teams within similar disciplines.

Seen from a company product perspective, the developed fuel cell system could potentially be incorporated into Modelon's Fuel Cell Library (FCL).

The overall question formulation, in line with the above, is thereby: To what extent can the developed model reproduce a realistic system behavior, when compared to available information and literature data and when simulated in established test drive cycles? By this, the model should be able to produce a realistic output during simulation, but also to capture the effects of changes of a wide range of operating conditions, such as internal temperatures, operation pressure and variations in humidity in the stack system. The system model should also take variations of ambient temperatures into consideration.

System Requirements

The system will be designed according to existing parameter data from car manufacturers. Since Toyota is the actor on the market providing the most available product data and model information, the simulation model will mainly be based on the Toyota Mirai hydrogen car. Hence, the aim is to construct and parameterize the model according to the Mirai as far as possible. However, this will not be completely feasible, since Mirai model data and model information is not fully accessible. Another limitation in this regard, is the shortage of available test data for comparison.

The work will be built from the FCL and a number of other libraries, from which several base components and similar system examples are available. A series of self-developed components will also be created in order to receive a complete system model.

Scope and Limitations

The work will start from an available full vehicle template model, shown in Figure 1.1, and focus on the design of two different sub-systems of the model. The main focus will be directed towards the stack system, including the membrane and fuel cell, the supply of hydrogen and air and also the cooling system. The other subsystem comprises the power-train, including the motor and battery models, and some control software. This implies that the vehicle, driver and drive cycle modules available from the template, will not need any further modifications.

In simulation and modeling, there will always be a trade-off between accuracy and simulation time. To decrease simulation time, reasonable assumptions were to be made to simplify the models whenever applicable. Unless relevant details regarding the construction of a component were known or if its exactness was not of importance for the modeling, simplifications were to be performed.

The different input variables would also only be subject to simulations within certain ranges. Simulating the model at ambient temperatures below zero degrees would be too complicated to implement, since it would require more advanced media models. Start-up conditions would be omitted and the stack system would be simulated starting at a determined operation temperature.

The hydrogen tanks or refueling is not a part of the scope, since this would require a real gas model due to the extremely high pressure (up to 700 bar) [Toyota,

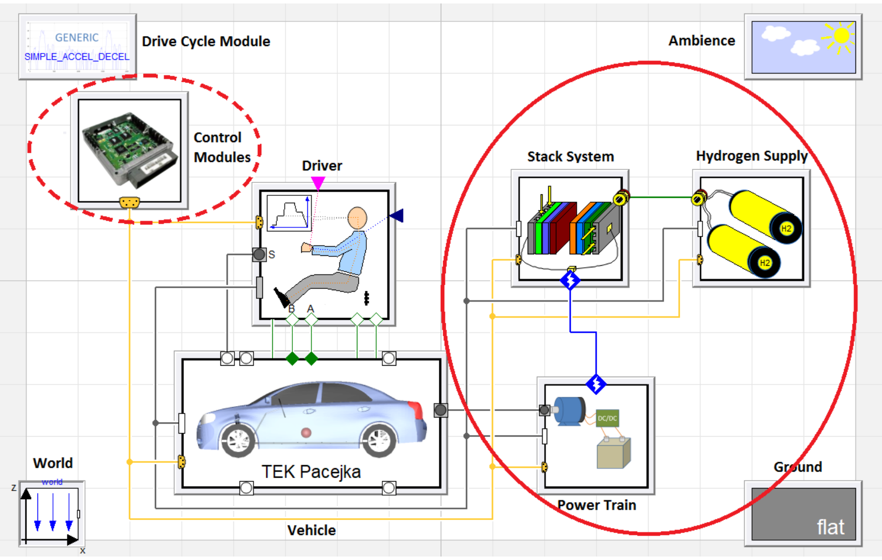

Figure 1.1 The Modelica template of the full FCHV system with the different modules and their connections. The circumscribed modules to the right are to be constructed in the thesis work. The control modules will also require some modification.

2016b]. Neither is material degradation of catalysts, electrodes or other equipment included in the model.

Contribution to Science and Development

Exchanging classical combustion motors in cars for electrical motors is a hot topic worldwide in the quest for more environment-friendly solutions. An electrical motor has an efficiency of up to 83 percent, while the combustion motor of a car can reach a maximum efficiency of about 18 percent [Emobility, 2017]. Electricity produced by hydrogen fuel cells would add even more advantages, since the only waste products are water and heat.

Within research and development in the car manufacturing field, it would be of great advantage to have detailed simulation models of these fuel cell systems as a tool when developing future efficient, safe and environment-friendly driving systems.

1.2 Theory

Fuel Cells

In the following, a brief introduction to fuel cell theory will be given, to improve the understanding of this work.

Fuel cells are electrochemical devices that convert chemical energy of a gaseous fuel directly into electricity [Pukrushpan, 2003]. A fuel cell consists of an electrolyte, sandwiched between an anode and a cathode electrode, thereby forming an anodic and a cathodic half-cell. In each of the half-cells, a cell reaction occurs, generating respectively consuming electrons and hence promoting an electric flow between the anode and the cathode [Larmine and Dicks, 2003].

Several types of fuels and oxidants are available for fuel cell applications, where the most frequently used is the hydrogen fuel cell [Larmine and Dicks, 2003]. In this cell, the fuel consists of hydrogen, which is oxidized by oxygen, thereby producing water and releasing energy. The overall electrochemical reaction, generating the thermodynamic potential on which the principle of the fuel cell is based, is given by [Amphlett et al., 1995]:

$$2H_2 \;+\; O_2 \;\rightarrow\; 2H_2O$$

During electricity generation, the only byproducts are heat and water. By this, the technique implies a potentially environment-friendly alternative of energy generation. For that reason, fuel cell technology is today developing at a rapid pace [Larmine and Dicks, 2003].

Several types of fuel cells exist and depending on their intrinsic properties, they are appropriate for different fields of applications. Decisive parameters may be migration ion type through the electrolyte and their operating temperature. Table 1.1 summarizes the most frequent types of fuel cells and their temperature range [Larmine and Dicks, 2003].

A common fuel cell system used in automobile applications, due to among other things its convenient operation temperature, is the polymer electrolyte membrane (PEM) fuel cell [Larmine and Dicks, 2003]. The PEM fuel cell, which is alternatively named proton exchange membrane fuel cell, is the cell type to be considered in this thesis work. Accordingly, in the following, the term “fuel cell” will refer to a PEM fuel cell, unless nothing else is stated.

PEM fuel cells possess high power density, longevity and are low-corrosive [Pukrushpan, 2003]. Hydrogen is provided by an external source and oxygen is normally supplied by the air. Since the cells operate at lower temperatures, it is required that the electrodes contain catalysts in order to increase the reaction rate [Larmine and Dicks, 2003]. Different platinum catalysts are the most common alternatives. The electrode backbone is composed of a highly conducting material, such as porous graphite [Pukrushpan, 2003].

Fuel Cell Type	***Operating Temperature***	***Applications and limitations***
Alkaline (AFC)	50-200°C	Space vehicles, requires environments free of CO_2.
Proton exchange membrane (PEMFC)	30-100°C	Vehicles, mobile applications, low power CHP (combined heat and power) systems. Requires high purity hydrogen.
Direct methanol (DMFC)	20-90°C	Portable electronic systems of low power. Limited cell power.
Phosphoric acid (PAFC)	~220°C	Larger CHP systems. Reformation equipment needed.
Molten carbonate (MCFC)	~650°C	Medium- to large scale CHP systems. Needs CO_2 to work.
Solid oxide (SOFC)	500-1000°C	All sizes of CHP systems. Requires complex helps systems.

Table 1.1 The table summarizes different types of fuel cells [Larmine and Dicks, 2003].

The membrane sandwiched between the electrodes consists of a solid polymeric electrolyte material. During operation, protons from the hydrogen (hydrogen ions, H^+) are released at the anode and migrate through the membrane towards the cathode, while the electrons flow through an external circuit. At the cathode, the protons and the electrons combine with oxygen to form water.

The membrane consists of Nafion, a polymeric material similar to Teflon. This material has a polytetrafluoroethylene backbone to which sulfonic acid groups (SO_3^- H^+) are attached. Nafion is an electronic insulator, but also an excellent conductor of hydrogen ions [Thomas and Zalbowitz, 1999]. The backbone by itself is water repellent, but water molecules associate to the sulfonic groups when the membrane becomes hydrated. During operation, protons are transported through the membrane by hitching onto water molecules that are moving through the membrane [Spiegel, 2008]. The water molecules are prone to leave the membrane and this implies that in order to work properly, the Nafion membrane must be continuously hydrated during operation. However, the compensating humidification process must be adequately controlled. A too dry membrane is a poor proton conductor and a flooded membrane will decrease efficiency and result in water condensing at the electrodes and inside the flow channels, thereby blocking them and deteriorating the cell operation [Larmine and Dicks, 2003].

The electrodes together with the membrane form a membrane electrolyte assembly (MEA), which is typically less than a millimeter thick. The MEA is enclosed between two backing layers, which ensure efficient diffusion of each reactant gas to the catalyst sites of the electrodes. These backing layers are pressed against flow field channel plates, which contain channel systems for providing reactant gas and

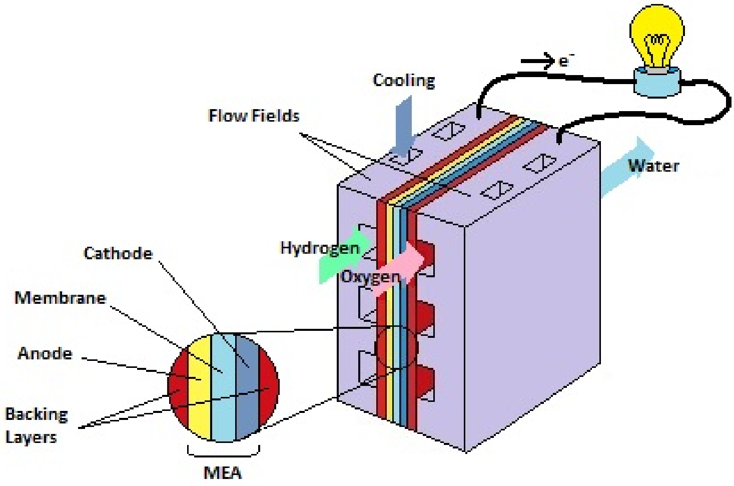

Figure 1.2 The picture illustrates the fuel cell structure and the flows through the flow channel plates.

for removing reaction water formed at the cathode. The flow field plates also serve as current collectors [Pukrushpan, 2003]. Furthermore, flow channels for cooling medium are incorporated in these plates [Larmine and Dicks, 2003].

As a consequence of the above, a complete fuel cell unit comprises not only air and hydrogen supply systems, but also cooling and water management systems. The system is illustrated in Figure 1.2.

Assuming ideal gas laws, the theoretical voltage produced by a fuel cell is given by the Nernst equation for the H_2/O_2 electrochemical reaction [Kabza. A, 2016]:

$$E = E^0 + \frac{RT}{2F}\ln\left(\frac{p_{H_2}p_{O_2}^{0.5}}{p_{H_2O}}\right) \tag{1.1}$$

In Equation 1.1, E^0 [V] is the standard cell potential, R [J/(K·mol)] is the universal gas constant, T [K] is the temperature, F [C/mol] is Faraday's constant and p [bar] represents the partial pressures of the reactants and products. However, during operation, fuel cells are subject to several kinds of losses, which lower the actual out voltage from the theoretical, thereby causing a voltage drop. The four most prominent causes of voltage drop are:

- *Activation Losses:* These losses result from the tardiness of the reactions taking place on the surfaces of the electrodes. A fraction of the voltage generated is lost by driving the electron transferring reactions. This type of losses have a logarithmic progression and cause the most prominent voltage drop in

PEM fuel cells. They appear at both electrodes, but in hydrogen fuel cells, the over-voltage at the anode is about a factor 10^4 less than at the cathode, and is therefore negligible in the equations below. In Equation 1.2, the current density drawn from the cell is represented as i [A/m^2], whereas i_0 [A/m^2] is called the *exchange current density*. The latter is the minimum value that i must exceed for the equation to be valid. Finally, α is the *charge transfer coefficient*, a reaction and material dependent constant varying between 0 and 1. [Larmine and Dicks, 2003]:

$$\Delta V_{act} = \frac{RT}{2\alpha F} \ln\left(\frac{i}{i_0}\right) \tag{1.2}$$

- *Fuel crossover and internal currents:* The ideal behavior of the electrolyte medium is to transport ions only (i.e. protons in the case of the hydrogen fuel cell) between the electrodes. This type of loss is caused by fuel migrating through the electrolyte and also, to a minor extent, from direct electron conduction through the electrolyte. These effects are most prominent in low temperature cells, like the PEM fuel cell, and especially when the electrolyte membrane thickness is small. The term representing this loss, the *internal current density* i_n [A/m^2], is normally incorporated in Equation 1.2, to give the following expression [Larmine and Dicks, 2003]:

$$\Delta V_{act} = \frac{RT}{2\alpha F} \ln\left(\frac{i+i_n}{i_0}\right) \tag{1.3}$$

- *Ohmic losses:* This type of voltage drop occurs simply due to the resistance to the flow of electrons through the material of the electrodes and the resistance to the flow of ions through the electrolyte. The size of these losses is proportional to the current density. To minimize this voltage drop, a well designed cell system is of importance. Electrodes should have the highest possible conductivity and appropriate materials should be chosen for the other parts of the cell. The electrolyte layer should be as thin as possible. The equation for this type of voltage drop is simple [Larmine and Dicks, 2003]:

$$\Delta V_{ohm} = ir \tag{1.4}$$

However, the area specific resistance, r [$\Omega\cdot$m^2], is given by a series of more advanced formulas [Pukrushpan, 2003], omitted here. The resistance has dependencies on for example humidity content of the membrane and membrane thickness.

- *Mass transport or concentration loss:* These types of losses are caused by the change in concentration of the reactants on the electrode surfaces during the transportation through the cell as the fuel is consumed. This is due to the inability to provide sufficient quantities of reactants to the electrode surfaces. The voltage drop is proportional to the pressure drop of the reactants over the cell and is given by the expression below, where i_L [A/m^2] is the physical maximum exchange current density [Larmine and Dicks, 2003]:

$$\Delta V_{trans} = -\frac{RT}{2F} \ln\left(1 - \frac{i}{i_L}\right) \tag{1.5}$$

In order to reach the voltage required to run an electric device, a plurality of fuel cells are connected in series, thereby forming a stack assembly, referred to as a fuel cell stack.

Within fuel cell development, it is often useful to plot the cell voltage against the current density, in order to receive a profile of its characteristics. A general V-I plot is displayed in Figure 1.3.

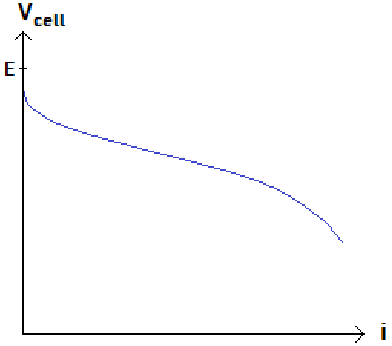

Figure 1.3 Cell voltage as a function of the current density for a fuel cell. As the current density increases, the gathered sum of the losses becomes more prominent. At higher current densities, the cell voltage begins to fall faster.

Hydrogen Driven Cars

State of the Art Hydrogen is successively gaining attention as a future alternative to traditional fossil fuels, due to its zero carbon dioxide emission during consumption and the possibility of producing it from a wide variety of energy sources in any region of the world [Nonobe, 2017].

The car industry currently has a great interest in electrification of vehicles. China, that for a long time has been in serious need of lowering emissions and improving air quality, is the leading nation in the number of battery and plug in hybrids. All leading car manufacturers either already have or plan to put battery, plug-in or fuel cell hybrid vehicles on the market within the next few years. The interest in using hydrogen driven fuel cell technology in the next generation of cars is most solid in Asia. Primarily Japanese and Korean manufacturers (Toyota, Honda, Kia, Hyundai) have ventured in FCHVs by the release of the models Toyota Mirai, Honda Clarity and Hyundai ix35 [Kristensson, 2017b]. This development can also be seen in the number of vehicles running. At the end of 2017, Sweden had 45 000 registered battery or hybrid vehicles and this number is growing exponentially [Power Circle AB, 2017].

Principles of the FCHV The fuel of the hydrogen car, i.e. hydrogen, is stored in and provided to the fuel cell from especially designed high pressure tanks. The pressurized hydrogen is transformed down to the magnitude of atmospheric pressure before being injected into the fuel cell system on the anode side.

The other reactant, oxygen, is simply provided from the surrounding air. The air is compressed and supplied to the fuel cell on the cathode side.

Due to the requirement of humidification of the membrane, in order to reduce its internal resistance to proton transfer, moisture has to be provided by the inflow of reactants. The most commonly described solution to this problem is to add an external humidifier, which mixes the inflowing gases with vapor prior to injection into the stack. An alternative, used in Toyota Mirai, is to integrate the humidifier functions directly in the stack, as an internal humidifier.

Since the operation of a PEM fuel cell is temperature critical, a water cooling system of the stack is required.

During cell operation, electricity is generated at the electrodes and is transfered to the power train of the system, where it is transformed into higher voltages. From here, the current can either be inverted into AC for supplying the motor or be converted to a lower voltage to be stored in the battery.

While braking the vehicle, the braking energy is transfered from the motor back to the power control unit, from where it is further transfered to and stored in the battery. During acceleration of the vehicle or in other situations when the fuel cell electricity supply on its own is not sufficient, extra energy is withdrawn from the battery, just like in other hybrid vehicles [Cipollone et al., 2015].

The basic operation principle of a hydrogen car is illustrated in Figure 1.4.

Pros & Cons of the Technology Fuel cell applications substituting traditional power systems provide several advantages [Larmine and Dicks, 2003]:

- *Efficiency:* Fuel cells and electrical motors are pre-eminently more efficient than combustion engines, whether piston or turbine based. A further feature within this technology is the ability of producing smaller systems that are just as effective as larger ones.

- *Simplicity:* Since fuel cell systems and electrical motors are simple and consist of few moving parts, wear and tear of the system is kept on a minimum level. Thereby, highly reliable and long-lasting systems are provided.

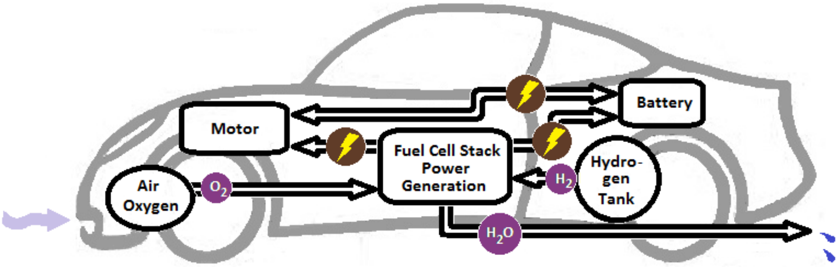

Figure 1.4 Oxygen and hydrogen are supplied to the fuel cell stack, where they react into water during the release of electric energy. The electricity is supplied to the motor, but can also be stored in the battery. The battery can provide extra energy to the motor, or inversely store braking energy.

- *Low emissions:* The only by-products of the main fuel cell reaction are water and heat, consequently implying a zero-emission at the point of consumption. This is the main advantage of fuel cells when being used in vehicles.
- *Silence:* Fuel cells operate very quietly, even if extended by extra fuel-processing equipment. This is of particular importance in portable power applications, as well as in combined heat and power systems.

However, since the technology is still in its cradle, fuel cell vehicles also have some major issues to be resolved:

- *Cost:* Mainly due to the fact that platinum is highly expensive, fuel cell technology is costly, although extensive research has managed to decrease the amount of platinum catalyst required [3M Company, 2016].
- *Production:* Production of sufficient quantities of hydrogen in an environment-friendly manor is required [Larmine and Dicks, 2003]. Different techniques are still under development, but are far from effective [Kristensson, 2017a].
- *Distribution:* Hydrogen distribution and refueling infrastructure must be secured and established [Chan et al., 2010]. For example, at the date of writing, only very few hydrogen gas stations are available in Sweden.

When performing the comparison of hydrogen powered fuel cell electric vehicles (FCEVs) and regular battery electric vehicles (BEVs), BEVs are found to have a shorter tank range, but on the other hand, have a lower price. This turns BEVs into a more economic alternative when only operation on shorter distances is required. The still less developed FCEV technology is capable of longer driving ranges (>500 kilometers). Although the possibility of fast-charging, a BEV takes considerably longer time to charge, while a FCEV can be refilled within minutes, just like an ordinary internal combustion engine vehicle (ICE) [Gröger et al., 2015].

Modelica and Dymola

Modelica is a non-proprietary programming language, developed for modeling and simulation of complex technical or physical systems. The language comprises libraries, containing different sets of subcomponents and building blocks. The hierarchical, object-oriented structure enables reuse of code. A powerful feature is the possibility of modeling the dynamic behavior of physical systems. The models are described by differential, algebraic and discrete equations and components are linked by different types of connectors. Modelica has been used in industry since year 2000 [Modelica Association, 2017]. Several free and commercial platforms are available for supporting Modelica, with Dymola being one of the latter.

Dymola is a development environment and a complete tool for modeling and simulation of integrated and complex systems. It can be used for engineering within automotive, aerospace, robotics, process and several other fields of applications [Dassault Systèmes, 2017]. Dymola models can be visualized both in graphical layers and as text. When editing in the graphical layer, the text layer will automatically be updated. Dymola also enables real time 3D animations during simulation.

2

Modeling

2.1 Scope and System Structure

Modeling work

This chapter describes the development of the model. This work was divided into different modules concerning various parts of the fuel cell vehicle system. Firstly, a simplified, but runnable model of the fuel cell stack system and the power train part of the system was built, in order to have a full system model with the most necessary functionalities. As a next step, two types of membranes were constructed, one containing electro chemical properties and one more advanced, also possessing water management functions. The flow channel plates, sandwiching the membrane

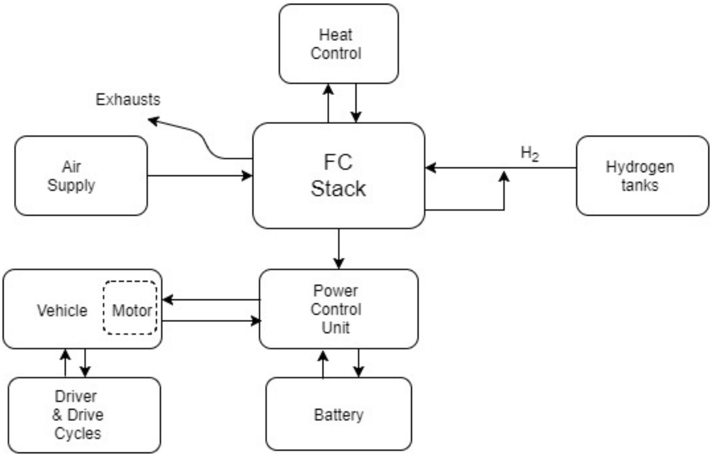

Figure 2.1 Block overview of the system. The fuel cell stack interacts with three auxiliary systems; air and fuel supply and the cooling system. The electricity generated is transfered to the power train, consisting of PCU, motor and battery. The arrows indicate exchanges between the units.

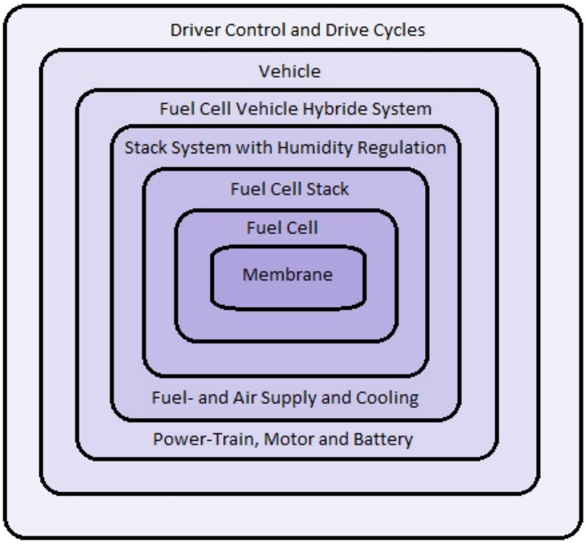

Figure 2.2 The membrane is the heart of the system, where the electrical energy is produced. The membrane is encapsulated by different layers which add functions to form a complete vehicle-driver system.

were also modified to be represented by far more complicated components. After completing the stack, the fuel supply system was extended to contain a humidifier component. Further, a more advanced cooling system of the stack was created. In the stack system, the different auxiliary devices were equipped with power consumption models and controllers were added. A control software module for determining how current was supposed to be drawn from the stack was also constructed.

System structure

The system to be implemented as a Modelica model, has the overall structure according to Figure 2.1. A more detailed system model is attached in the appendix section, Figure 7.2. The most delicate part of the system is the fuel cell membrane, into which the electrode functionalities are merged. By the membrane's ability to determine the electricity generation, power characteristics and limitations, the membrane is the most fundamental part of the system, as illustrated in Figure 2.2. The membrane model is included in a fuel cell, also comprising the flow channel plates that supply the reactants, remove the reaction water and provide cooling channels. In the Mirai model, 370 fuel cells are connected in series, thereby forming a stack.

This stack is included in a stack system, also consisting of air and hydrogen supplies and water cooling. The anode side of the stack is shaped as a loop for recirculation of unconsumed fuel. Auxiliary components, such as an air compressor and a humidifier are also included on the cathode side of this stack. The power generated by the stack is transfered to a power control unit (PCU). A boost converter in the PCU increases the stack voltage from about 200-400 V to 650 V, which is the fixed voltage demanded by the Mirai motor. Before entering this motor, being an AC motor, the DC current is converted into AC. Excessive energy from the stack and braking energy from the motor is transformed through a buck converter from 650 V to about 245 V for storing in the battery. Inversely, when required, extra energy to the motor can be withdrawn from the battery.

The vehicle model further contains components such as chassis, wheels and steering system and the driver model possesses functionalities such as acceleration, braking and steering. The vehicle-driver template comprises exchangeable drive cycle tests, which are modules that mimic different driving patterns such as accelerations, decelerations and braking during highway or city driving. The full FCHV model also contains modules declaring ambient conditions such as temperature, gravitation, ground declination and wind. (The latter modules are illustrated in the corners of the Modelica template, Figure 1.1.) As mentioned earlier, the complete models of vehicle, driver and ambiance are implemented and parameterized in the Vehicle Dynamics Library (VDL) and are not a part of the intended task.

The available template in the FCL was runnable, but consisted of a very basic and also different type of fuel cell vehicle system. This was built on reformat technology, implying that methanol is degraded into a gas mixture of hydrogen and carbon-dioxide, before being injected into the fuel cell stack. The stack system only contained simple solutions by ideal flows of air, fuel and cooling water. The powertrain system also had a different design, a DC motor instead of an AC motor and another type of battery than the Mirai. Due to this, the model was very different from the model to be built in this project. However, it contained a series of useful components and models that could be rebuilt and extended per requirements.

2.2 Simple System Model

As a first task, a simple model of the stack system and the electric drive was built from similar models and additional components available from different libraries. This model was integrated in the available FCHV system template (displayed in Figure 1.1) and was thereby able to perform drive cycle tests.

The purpose of this model was not only to acquire a deeper understanding of the FCHV system, but also to achieve a complete starting model that could convert the reactants into electricity, heat and water and transport an electric current through the system to the motor module to power it. The simple system model was to serve as a base model, to be completed with additional components, functions and control units along the thesis work.

Principle

The simple system model consists of two modules; the stack system and the electric drive system. These systems were developed separately and were finally merged into the full FCHV system template. The different components were implemented and parameterized individually in simple test experiments, before being integrated into the system model. The modules were retested in each iteration of the model development. Auxiliary components were either omitted or implemented in a simple or ideal way. Ideal in this sense implies that no losses or fluctuations are taken into regard.

The stack system consisted of a fuel cell stack with air and hydrogen supply and water cooling. The electric drive system was assembled from a motor, a battery and two DC/DC converters.

The structural model of the simple system is illustrated in Figure 7.1 in the appendix section.

Implementation

Stack System The structure of the sub-stack is displayed in the right part of Figure 2.3. The membrane built according to Section 2.3, was already prepared and available and was therefore incorporated in the stack model. In a physical stack system, the fuel cells are connected in series to reach the desired stack voltage. While modeling, this is implemented by a multiplier, n, representing the number of cells in the stack component, where the voltage generated and the amounts of reactants and byproducts consumed and produced by one cell are multiplied by n.

The flow channel plates for air and fuel, surrounding the fuel cell were modeled by two already available lumped condensing volumes, one at the cathode and another at the anode. In these components, the flow channels are simply represented as a volume with three ports, connecting to the reactant in and outlets and to the membrane component and through which gases can be transfered. Inside the volumes, liquid water can evaporate, and inversely vapor can condense into liquid water. Water is only able to leave the volumes while in gas form.

The stack template was equipped with a cooling pipe with an adjustable active area facing the sub-stack for heat exchange between the stack and the cooling water. The sub-stack and pipe are displayed in the right part of Figure 2.3. The cooling pipe is connected to an ideal pump of cooling water (modeled by a source component of ideal mass-flow) and a sink boundary for outflowing water (i.e a component representing an ideal outlet drain of infinite volume) visible in Figure 2.4. The cooling water flow was adjusted to keep the stack temperature at 70-80°C at steady state.

The rest of the stack system, described below, is illustrated in Figure 2.4. A source of humidified air was connected to a compressor component and air was compressed into the stack. Temperature regulation and further humidification were

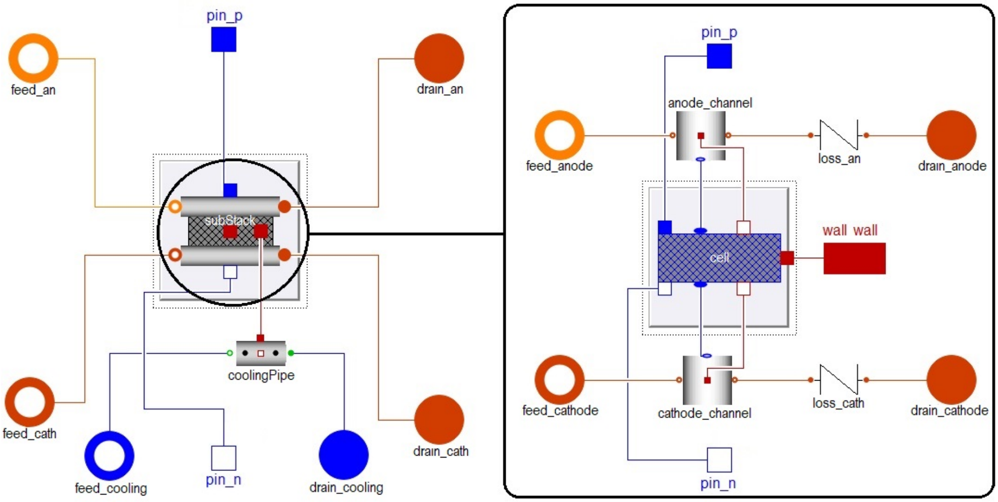

Figure 2.3 To the left, the inside of the stack component (shown in Figure 2.4) reveals a sub-stack, which is connected to a cooling pipe and different types of connectors represented by circles and squares. To the right, the inside of the sub-stack is displayed. The membrane (named "cell") in the middle is connected to the anode and cathode channels, represented by condensing volume components. The two loss components connected to the volumes handle pressure drop across the system.

omitted. Since the simple system model was lacking a humidifier, the model was run with air of adequately high humidity, to still get a satisfying fuel cell performance. The air was passed through the fuel cell and was led out through the cathode and into a sink boundary.

Hydrogen from an ideal hydrogen source of fixed pressure was let into a recirculation system via a valve. The hydrogen was passed through the fuel cell and the residual hydrogen was recirculated in a loop and was fed back to the inlet, where the corresponding amount of consumed hydrogen was added though a valve to reach the desired pressure. By this construction, the unconsumed hydrogen was recycled and no after-burner was required. Thereby, fuel efficiency was increased and no residual hydrogen was emitted into the atmosphere. As a simple solution for adjusting the hydrogen valve, a P-controller was implemented. It was modeled by a gain component and a feedback component.

The mass flow in the recirculation loop was maintained by the implementation of a fan. (In the Toyota Mirai, a blower is used for this purpose, and the fan is the

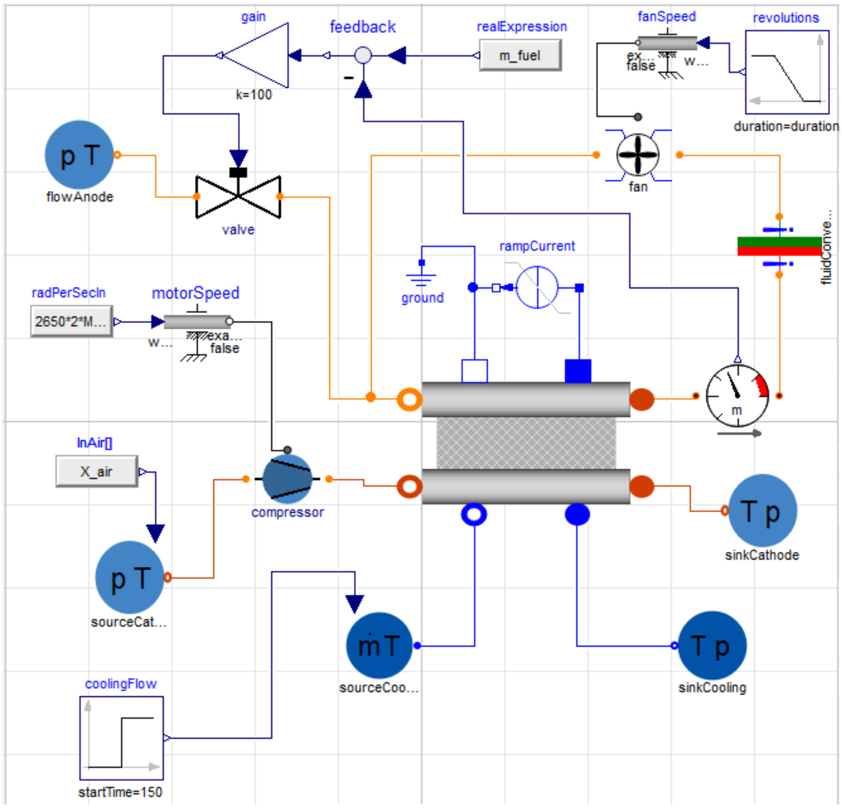

Figure 2.4 Simple stack system, which was the first version of the stack system model. The stack in the middle of the figure comprises the sub-stack and the cooling pipe from Figure 2.3.

closest equivalent component available among the library components. [1])

The compressor and the fan were set to a constant rotational speed, preparing for a next step where efficiency tables to decide the power consumption of the device were to be implemented in the components.

In Modelica, all components including a volume will require a medium model to calculate thermodynamic properties and transport properties of the fluid. Different medium models have difference assumptions such as: single phase or two phase, pure fluid or gas-liquid mixture, reacting or non-reacting etc. The assumptions of the medium models must be consistent with the component models that use them

---

[1] The difference between the two components is that the blower circulates the gas only on a specific area, while a fan distributes the gas flow over a wider space. Since the component considered operates inside of a smaller pipe, the difference is assumed to be neglected.

for property calculations. For that reason, when transferring a medium through a system of components, medium conversion components might be required. In the stack system, three medium conversion components were needed, whereof one is visible in Figure 2.4 and the others are integrated at the anodic and cathodic entrances of the stack. A condensation medium is required inside of the stack, since this is able to handle water both as steam and in liquid form and also to convert water between these two aggregation forms. However, two phase properties are not applicable inside of components such as compressors or fans, handling gases exclusively.

Power Train System For the power train part of the system, several kinds of inverters, converters and motors were available from different libraries. For inverters and converters, switch components similar to those used in real systems were desired. Components chosen from the FCHV and FCL libraries would be the best choice, since they were rather simple, but still containing the basic physics required for the intended type of systems. More detailed physical models were considered to be less suitable, since they might introduce undesired high frequency response that was not within the scope of the physics to be captured by the model.

In the components chosen, the loss could be set to a percentage, or if desired, be calculated according to different tables implemented in the components.

The Toyota Mirai has a synchronous AC motor, so the initial intention was to implement an AC motor component preceded by an AC/DC inverter in the power train model together with some control logic. However, to meet the requirements of the motor model, the necessary gathered functions from the AC motor, the inverter and the logic, could simply be lumped into a single DC motor component.

Using a simple AC motor and an inverter would make the Dassl solver (the standard solver in Modelica) extremely slow and unable to finish within reasonable time. This was due to some demanding processing during the three phase AC calculations. Further, modeling the motor as an AC motor plus an inverter would be rather complicated, since these models would function quite differently from a DC motor. The parameterization would require to be translated into other variables (such as current, pole pares and inductance) than the torque parameters available from the Mirai data sheets [Toyota, 2016a] (ω_{max}, τ_{rated} and P_{rated}). Since many other help parameters that would be required were missing, several assumptions of parameter values would have to be performed. Due to this, the final AC model would not have greater exactness than the original DC model and also slow down the simulation speed substantially. Since the objectives of the model to be built did not include the study of three phase AC current, the simpler DC motor would be perfectly adequate.

The battery was the simplest component in the power-train system. It was modeled as a passive component, with no control logic of its own. By this, the battery would simply work as a buffer of electricity, from which current was either withdrawn, or into which current is stored, depending on the demands from the logic of surrounding components. Thermal effects of the battery was not considered.

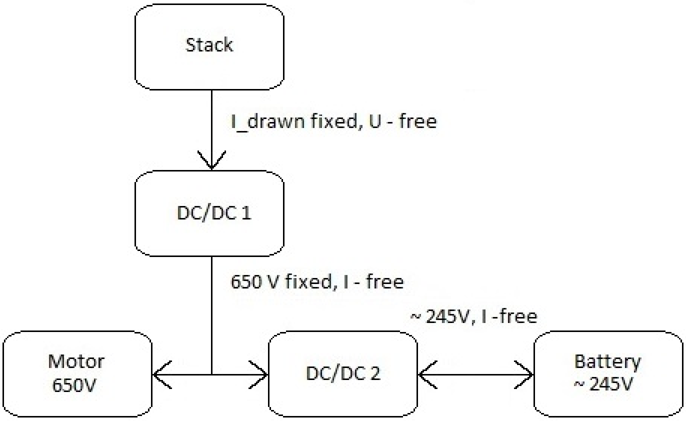

Figure 2.5 Between the stack and the first DC/DC converter, I_{drawn} is determined by the control software of the DC/DC converter. The second DC/DC converter determines the voltage to the motor. Between the second converter and the battery, the voltage is directed by the battery.

The most important parts of the battery component were the *cell-data record*, containing relevant data for the respective type of cell, and the parameters for the number of cells in series and in parallel. Data for the nickel metal hydride battery cell was taken from literature [Energizer, 2010] and from similar battery models in the VDL. The number of cells in series required to reach the desired battery voltage of 245 V [Cunningham, W., 2014] was calculated. The number of required cell rows in parallel was adjusted by simulating the battery in a power-train model test, to find an appropriate robustness for the system, where the changes in voltage and current depending on the drive cycle demands did not become too aggressive, since very large numerical derivatives would interrupt the simulation. When the battery was incorporated in the full system model, the number of parallel cells had to be increased even further to give the model sufficient robustness.

The two DC/DC converters in the power train were to ensure the correct voltage in the different sections of the system. The converter construction implied that for each of the converters, either one of the currents or one of the voltages would be set as directive, while the other variables were free to vary according to the physical power law

$$P = V_1 \cdot I_1 = V_2 \cdot I_2 \tag{2.1}$$

and the demands from other parts of the system. The converter functions are illustrated in Figure 2.5.

The boost converter, which increases the voltage, used the current drawn from the stack, which was determined by the control software, as the directive variable. The outgoing voltage would then adapt to the 650 V level demanded by the second

Parameter	***Input Value***
Cell temperature [°C]	80
H_2 supply [mole % H_2]	100
Air supply [mole fractions]	[H_2O:N_2:O_2]; [0.161, 0.663, 0.176]*
H_2 pressure [kPa]	150
Air pressure [kPa]	250
Number of cells, *n*	370

Table 2.1 The different input parameters for the stack system model derivation. *This corresponds to a RH of 85 %.

converter, while the outgoing current was free to vary according to the power. The voltage and current on the battery side of the second converter were unregulated by the converter, but the voltage had to adapt to the requirements of the battery. The battery model demanded about 245 V, however this voltage varied slightly with the state of charge (SOC) of the battery, that is the actual charge level.

An available template of a similar power-train system was redesigned to meet the structure of the new system, and from this, a power-train test module to be used for the development was also created.

The battery model and the second converter, of which the latter was implemented as a modified version of an available converter component, were first tested individually and then together, before being transfered to the full system model with the stack system and an available boost converter component (DC/DC1), as illustrated in Figure 2.5.

Parameterization

Stack system Throughout the development, the stack system, the power train system and the full FCHV system were tested by ramping the stack current up from 0 to 300 A during 300 s, after which the current was held at a constant 300 A until 3000 s. By this, both the transient behavior and the steady state at a reasonable operating point could be monitored.

The input parameter data was chosen according to available Toyota Mirai information sources [Toyota, 2016a], [Toyota, 2016b]. Dry air was estimated to consist of 21 mole % oxygen and 79 mole % nitrogen. Since the fuel cell requires at least 85 % RH on the incoming air in order to operate optimally, the air composition was adapted accordingly by the implementation of an available Modelica function. The input parameter data in Table 2.1 was chosen.

P-regulator The mass flow of hydrogen into the stack is the sum of hydrogen already present in the loop plus the hydrogen added through the valve. This total flow was set to 0.01 kg/s, with is a reasonable flow for a system of this size [Larmine and Dicks, 2003]. This inflow to the stack subtracted to the measured outflow gives the quantity of hydrogen consumed. The hydrogen consumption is the input to the gain directing the valve opening, varying between 0 and 1. Since the theoretical maximum consumption of hydrogen is 0.01 kg/s, the k-value of the P-regulator was set to 100 in order to properly control the valve opening.

Parameter	***Designation***	***Value***
Rated maximum speed [rad/s]	ω_{max}	340
Maximum torque [N m]	τ_{rated}	335
Maximum power [kW]	P_{rated}	113
Nominal voltage [V]	$V_{dc\ nominal}$	650

Table 2.2 Parameters of the torque component of the DC motor [Toyota, 2016b].

Power Train The DC motor was parameterized according to Table 2.2 and the battery according to Table 2.3.

Parameter	***Value***
Number of cells in series, *ns*	164
Number of parallel cells, *np*	10
$V_{cell\ min}$ [V]	1.0
$V_{cell\ max}$ [V]	1.5
$V_{cell\ nom}$ [V]	1.2
R_{cell} [Ω]	0.003
Q_{cell} [C]	7024

Table 2.3 The number of cells of the battery pack and the parameterization used in the cell info data of the battery [Energizer, 2010].

The charge of a battery cell, Q_{cell} was calculated from the energy capacity of the battery, which is 1.6 kWh [Cunningham, W., 2014] [Pihl, J., 2014] and by the formulas given in Equations 2.2 - 2.5 [Eric Durling, 2017].

The total battery energy, W_{batt} [J] is proportional to the the single cell energy and the number of cells:

$$W_{batt} = W_{cell} \cdot ns \cdot np \tag{2.2}$$

The total battery voltage range, V_{batt} [V] is calculated from the voltage range of the cell, i.e. the difference between $V_{cell\ max}$ and $V_{cell\ min}$, which is equal to 0.5 V. V_{batt} is only dependent on the number of cells in series and not in parallel:

$$V_{batt} = V_{cell} \cdot ns \tag{2.3}$$

Q_{cell} [C], is derived as:

$$Q_{cell} = \frac{W_{cell}}{V_{cell}} = \frac{W_{batt}}{V_{batt} \cdot np} = \frac{W_{batt}}{V_{cell} \cdot ns \cdot np} \tag{2.4}$$

Hence,

$$Q_{cell} = \frac{1600Wh \cdot 3600s/h}{0.5V \cdot 164 \cdot 10} = 7024 \text{ C} \tag{2.5}$$

2.3 PEM Fuel Cell

In this part of the project, two new membranes were to be built. The first membrane was a simplification of the *ElectroChem* membrane available in FCL. The second membrane was an extension of the first membrane, where equations for water management and moisture dependence of the membrane were added.

Principle

When modeling fuel cells, it is important to understand the fundamental differences between how a physical fuel cell and a fuel cell model is designed. In a physical fuel cell, the electrodes and the electrolytes are separate components with different functions. The component which in the model is referred to as "membrane" is in the physical fuel cell rather an MEA, handling electricity generation, proton transport and water management. In the model, the gas getting in contact with the edge of the membrane component via the flow field channel ports, will immediately also be available with the same concentration and composition to any of the functions of the MEA. In the physical fuel cell, these substances will first diffuse through the porous electrode, to reach the electrolyte membrane surface.

The model structure was chosen due to the simplicity of merging three components into one, although the difference in diffusion mechanisms may have some effect on the overall fuel cell behavior.

The available *Electro Chem* membrane was based on the Nernst equation (Equation 1.1) and the loss equations introduced in the fuel cell theory chapter. In these equations, both the Nernst potential and the losses were temperature dependent.

The second membrane, from now on referred to as the *Water Transport* membrane, would build on to the first membrane with water transport included. As mentioned earlier, a controlled humidity level of the membrane was essential.

The reaction water forming at the cathode and the moisture provided by the inflowing gases hydrate the membrane, keeping the proton conductivity at a high level. Since reaction water is formed at the cathode, the water concentration tends to be higher on this side of the membrane.

Water transport across the membrane is balanced by two reversed forces; *electro-osmotic drag* and *back-diffusion*. While traveling across the membrane from anode to cathode, protons tend to transport water molecules, a phenomenon referred to as osmotic drag. Back-diffusion moves water molecules in the opposite direction, from the cathode towards the anode, and originates from the gradient of water concentration across the membrane. The two flows occurring from these forces will add up in one net flow, which is most often directed out of the cathode [Pukrushpan, 2003].

For simplicity, the mean value of the water content at the anode and the cathode would be assumed to represent the membrane water content [Pukrushpan, 2003].

Implementation

First Membrane The membrane is based on the assumption that the activation loss parameters i_0 [A/m^2] (the exchange current density) and i_n [A/m^2] (the internal current density) are constant. However, in reality, they are functions of temperature.

The formula for calculation of the concentration loss (Equation 1.5) could be simplified by instead using the constant values m [V] and n [A/m^2] [Kim et al., 1995].

$$\Delta V_{trans} = m \cdot \exp(ni) \tag{2.6}$$

The cell voltage was calculated according to:

$$V = E - \Delta V_{ohm} - \Delta V_{act} - \Delta V_{trans} \tag{2.7}$$

For the new membrane, the complete formula thus became:

$$V = E - ir - \frac{RT}{2\alpha F} \ln\left(\frac{i + i_n}{i_0}\right) + m \cdot \exp(ni) \tag{2.8}$$

The parameters i_0, i_n, m and n can be extracted by fitting the curve of Equation 2.8 towards a reference curve of the cell voltage by modifying the parameters.

Curve fitting, testing and validation was performed in a simple membrane test. For reference, a voltage plot of the *Electro Chem* membrane according to the conditions in Table 3.1, describing the stack system parameters was used. In the new membrane, from now on referred to as the *Electro Chem Simple* membrane, the implemented parameters i_0, i_n, m and n were adjusted in order to match the reference curve.

A formula for calculating the voltage efficiency was also added to the membrane code:

$$\eta_{Voltage} = \frac{V_{cell}}{E_l^0} \tag{2.9}$$

V_{cell} [V] is the cell voltage received and E_l^0 [V] is the standard potential for the lower heat value (LHV) [2] [Kabza. A, 2016].

The component was tested in a membrane test and in a stack test and was validated according to Section 3.1.

---

[2] Higher heating value (HHV) is the amount of heat produced during the complete combustion of a unit quantity of fuel. LHV is received by subtracting the latent heat of vaporization of the water vapor formed by the combustion from the HHV [The engineering toolbox, 2016].

Water Transport Membrane As mentioned above, this task was performed by adding a series of equations for diffusion and water flow to the code of the *Electro Chem Simple* membrane model and then testing it in different test models.

The membrane water transport model processes humidity content and mass flow of water into and out of the membrane. The water content and mass flow rates are dependent on current drawn from the stack and humidity of the reactant gases provided.

The net water transport through the membrane is provided by two formulas. Firstly, the water flow rate from anode to cathode based in the electro-osmotic drag is given as:

$$N_{v,osmotic} = n_d \frac{i}{F} \tag{2.10}$$

$N_{v,osmotic}$ [mol/(s·m^2)] is the water flow rate in one cell, n_d is the electro-osmotic drag coefficient, i [A/m^2] is the stack current density and F [C/mol] is Faraday's constant.

Approximating the concentration gradient across the membrane to be linear, the back-diffusion flow rate from cathode to anode is given by the second formula:

$$N_{v,diff} = D_w \left(\frac{c_{v,ca} - c_{v,an}}{t_m} \right) \tag{2.11}$$

$N_{v,diff}$ [mol/(s·m^2)] is the water flow rate in one cell, $c_{v,x}$ [mol/m^3] is the water concentrations at the anode respectively the cathode defined below, t_m [m] is the thickness of the membrane and D_w [m$^2/s$] is the diffusion coefficient of water in the membrane.

The combined expressions for the water transports, provide the net mole flow rate per unit area, $N_{v,membr}$ [mol/(s· m^2)], directed from the cathode towards the anode:

$$N_{v,membr} = N_{v,diff} - N_{v,osmotic} \tag{2.12}$$

Having the flow rate of water per unit area for one fuel cell, the total stack mass flow rate across the membrane, $W_{v,membr}$, can be calculated:

$$W_{v,membr} = N_{v,membr} \cdot M_v \cdot A_{cell} \cdot n \tag{2.13}$$

Here, M_v [g/mol] is the vapor molar mass, A_{cell} [m^2] is the cell area and n is the number of cells in the stack.

For the calculations above, a series of parameters from expressions given below, are required. The first factors required are the activities of the vapor at the anode, respectively the cathode. Activities are concentration dependent and for gases this implies that the activity is dependent on the reactant's partial pressure. For vapor, the activity also corresponds exactly to the relative humidity:

$$a_i = \frac{p_{v,i}}{p_{sat,i}} \tag{2.14}$$

The index i represents either anode *(an)* or cathode *(cat)*, $p_{v,i}$ is the vapor partial pressure and $p_{sat,i}$ is the saturation pressure at the present medium temperature.

Based on the activities and coefficients received from experimental result gained from Nafion membranes, the water content, λ_i, in different parts of the membrane can be calculated [Springer et al., 1991]:

$$\lambda_i = \begin{cases} 0.043 + 17.81a_i - 39.85a_i^2 + 36.0a^3 & , \ 0 < a_i \leq 1 \\ 14 + 1.4(a_i - 1) & , \ 1 < a_i \leq 3 \end{cases} \tag{2.15}$$

Here, the subscript i represents either anode *(an)*, cathode *(cat)* or membrane *(m)*, and a_m is approximated as the mean value of the activities at the two electrodes:

$$a_m = \frac{a_{an} + a_{cat}}{2} \tag{2.16}$$

The electro-osmotic drag coefficient, n_d, and the water diffusion coefficient, D_w, are then calculated from the average membrane water content, λ_m [Dutta et al., 2001]:

$$n_d = 0.0029\lambda_m^2 + 0.05\lambda_m - 3.4 \times 10^{-19} \tag{2.17}$$

and

$$D_w = D_\lambda \cdot exp\left(2416\left(\frac{1}{303} - \frac{1}{T_{cell}}\right)\right) \tag{2.18}$$

where

$$D_\lambda = \begin{cases} 10^{-6} & , \ \lambda_m < 2 \\ 10^{-6}(1 + 2(\lambda_m - 2)) & , \ 2 \leq \lambda_m \leq 3 \\ 10^{-6}(3 - 1.167(\lambda_m - 3)) & , \ 3 < \lambda_m < 4.5 \\ 1.25 \times 10^{-6} & , \ \lambda_m \geq 4.5 \end{cases} \tag{2.19}$$

The water concentrations at the membrane anode and cathode surfaces are functions of the membrane water content

$$c_{v,an} = \frac{\rho_{m,dry}}{M_{m,dry}}\lambda_{an} \tag{2.20}$$

$$c_{v,ca} = \frac{\rho_{m,dry}}{M_{m,dry}}\lambda_{ca} \tag{2.21}$$

Here, $\rho_{m,dry}$ [kg/cm^3] is the membrane dry density and $M_{m,dry}$ [kg/mol] is the dry equivalent weight of the membrane.

Equations 2.10 - 2.21 are taken from the PhD thesis work of Pukrushpan [Pukrushpan, 2003].

In the original *Electro Chem* membrane and its stack model, it is assumed that no water is entering the membrane through the anode side. This implies that water management is only handled on the cathode side, where water is either entering as humidity with the incoming air or is formed in the cell reaction.

Since water will now be able to pass in both directions across the membrane, the mass balance port equations connecting the membrane with the flow field channel component have to be modified to include water management also on the anodic side.

The boundary equations determining the mass and energy transfer into and out of the anodic membrane also have to be modified to additionally handle water transfer. The vector $MX_{flow,an}$ holds the information of the quantities of the different gases composing the entering anodic gas mix. Due to the definition of the flow direction of water, water data has do be added with a negative sign:

$$MX_{flow,an} = if\ \ index_{an[i]} == index_{H2}\ \ then\ \ m_{flowH2}\ \ elseif\ \ index_{an[i]} == index_{H2O}$$
$$then\ \ -m_{flowH2O,membr}\ \ else\ \ zeros(N)\ \ for\ \ i\ \ in\ \ 1:ns \tag{2.22}$$

The scalar, $m_{flow,an}$, represents the total flow into the membrane:

$$m_{flow,an} = m_{flowH2} - m_{flowH2O,membr} \tag{2.23}$$

The third port equation handles the total enthalpy flow through the port:

$$H_{flow,an} = h_{H2} \cdot m_{flowH2} - h_{H2O} \cdot m_{flowH2O,membr} \tag{2.24}$$

where h_x [J/kg] is the enthalpy for the respective fluid.
By this, the water management part of the membrane was completed according to physical mechanisms and boundary conditions.

Parameterization

The membrane parameter data derived from the curve comparison is given in Table 2.4.

Parameter	***Value***
i_0 $[A/m^2]$	0.22
i_n $[A/m^2]$	15
m $[V]$	$6.3 \cdot 10^{-3}$
n $[m^2/A]$	$6.0 \cdot 10^{-4}$

Table 2.4 Derived parameters for Equation 2.8.

2.4 Fuel Cell Stack

The first part of the water management of the stack is the water diffusion processes of the membrane, which have already been described in the Fuel Cell modeling chapter, Section 2.3.

In the second part of the water flow model, the purpose was to develop a new flow field channel component that includes physics for both vaporization and condensation processes.

In order to get a detailed picture of the important water management of the stack, the channel components were to be exchanged from the earlier used condensing volumes to discretized condensing pipe components. There were two main differences in functionality between these models. In the first component, the channel system was lumped into one single volume, while in the latter, the channels would instead be discretized into several sub-volumes connected in series.

In the condensing volume, liquid water is taken out of the system according to an equilibrium equation, while in the pipe component, the condensation is described by a correlation based on heat-and-mass transfer analogy.

Principle

In the fuel cell stack, reactant gases flow into the electrodes via the flow channels of the flow field plates, as earlier illustrated in Figure 1.2. The supply channels may have various shapes, but are always extended along the surface of the MEA to have an active surface facing it. Via the channels, the gases diffuse into the cell successively, while being transported parallel to the surface of the cell. Simultaneously, reaction water vapor, formed at the cathode, diffuses into the cathodic flow channel. The residual gases continue through the flow channels and exits the stack.

During its transport through the flow channels, two processes may occur to the water. Vapor may condense, and inversely, condensed water may evaporate. These phenomena are dependent on the stack temperature, the pressure and the fraction of water in the channel.

Condensed water in the flow channels may partially block the active cell area and also inhibit the gas flow through the channels, thereby decreasing the cell performance. For that reason, it is important to consider the amount of liquid water in the system when modeling, particularly in the more humid cathode channels.

Just as in all modeling, for proper modeling of the fuel cell stack water management, reality has to be simplified by a series of assumptions [Kabza. A, 2016]:

- All product water is removed via the cathode side, thereby implying that there is no water removed at the anodic side.
- The incoming gases are heated to a specific temperature inside the stack, which does not necessarily equal the stack cooling outlet temperature.
- All gases can be estimated to behave according to ideal gas laws.

Implementation

Discretized Condensing Pipe Approach The objective of the task was to develop a new component to capture different transport phenomena like gas diffusion, condensation, vaporization and heat transfer in the cathode respectively the anode channel. Different existing models from the libraries were taken as reference:

- A three port *Flow Channel Mass* pipe model, equipped with an extra mass flow port, handling gas diffusion exchange with the membrane.

- A *Reaction Channel* pipe model handling mass and energy processes occurring during different reactions in the flow mix.

- A discretized condensing channel model, *Distributed Channel Moist Air*, in which the condensation rate depends on the mass gradient between the vapor fraction of the flow and the equilibrium vapor fraction at the wall temperature. This mass gradient in its turn, is dependent on the temperature difference between the mass flow and the wall.
  Discretization into sub-volumes is particularly useful when conditions, such as temperature or concentration, vary significantly across the component.

- A lumped *Condensing Volume*, where uniform properties are assumed across the channel. Water is transfered from the gas via a separation process and is taken out according to a time constant. The condensation is instantaneous, which implies that the mixture is always in thermodynamic equilibrium. The model also allows particles of liquid water to be transported by the gas flow.

From these components, several attempts were performed to develop a discretized component containing functions for handling condensation, vaporisation and gas diffusion into and out of the cell. The implementation turned out to be more complicated than expected. Due to incompatibilities of the different pipe components and the medium models, integration failed.

Instead of deeper explaining Modelica specific details about the issues and limitations of the different components, focus will be aimed towards the physical mechanisms involved in the development of the final component.

Lumped Condensing Volume Approach This time, a lumped condensing volume component was chosen as a starting model. To this, a multiple choice function of different condensation models were implemented.

The first choice was a mathematical model, where water was taken out of the system according to a time constant, thereby mimicking a water separator principle. The second option was a physical model with the condensation driven by a concentration difference between the equilibrium at wall temperature and the current state in the flow. This driving force is equal to the one described for the reference component *Distributed Channel Moist Air*. These two models plus a third option, where formation and removal of liquid water were simply disabled, were implemented starting from the already available *Condensing Volume* component. In the dialogue window of the component, the different alternatives could be selected.

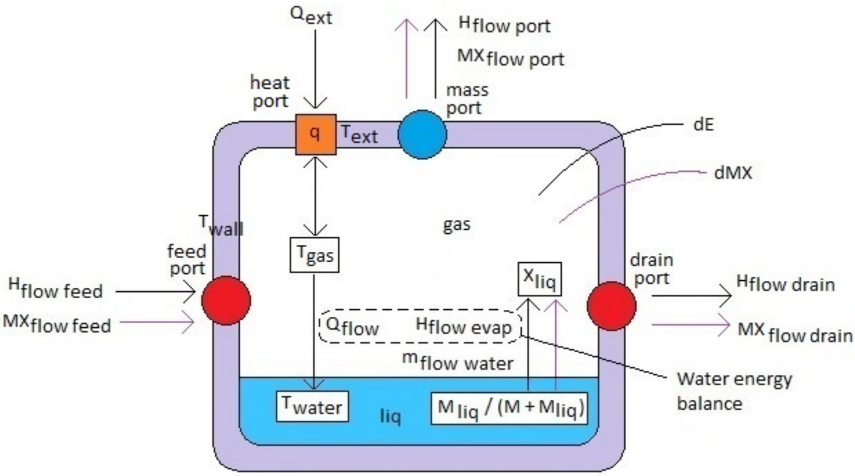

Figure 2.6 The separator principle model, from which the balance equations can be derived.

Separator System Model This model describes the water management of the flow field channels as a water separation process rather than water condensation. For improved understanding of the model, its assumptions and its interference with the environment, the system is illustrated in Figure 2.6. The component volume is considered constant and ideal mixing of the fluid in the volume is assumed.

It is necessary to keep track of incoming and outgoing mass flows and heat flows associated with the respective masses. All energy and mass flows across the component boundary are transfered via the existing connectors; the fluid ports and the heat port.

Through the feed port, a mass flow MX_{flow}, accompanied by its enthalpy flow, $H_{flow,feed}$, enters the component. In the same way, mass flows and enthalpy flows exit through the drain port and the mass port (of which the latter will be connected to the membrane). The external heat flow from an external heat source, Q_{ext}, forms a heat flow through the heat port, q. The temperature of the heat port, T_{ext}, is equal to the wall temperature, T_{wall}, and to the fluid temperature, T_{gas}. The sensible heat flow, Q_{flow}, is the heat flow from the gas phase to the liquid phase and affects the water temperature, T_{water}.

The fraction of liquid water carried by the gas stream, X_{liq}, is driven by mass fraction of liquid water separated from the gas in the volume. The flow of evaporated water, $m_{flow,water}$, (or in the opposite direction, flow of condensed water,) transfers liquid water between the liquid and the gas phase. This water flow is also accompanied by an enthalpy transfer, $H_{flow,evap}$.

Once this system overview is clear, balance equations of energy and mass flows can easily be derived. By these, both static and dynamic behavior of the model can be monitored.

The energy flow balance equation is derived as:

$$dE = H_{flow,feed} - H_{flow,drain} - H_{flow,port} + Q_{ext} - Q_{flow} + m_{flow,water} \cdot h_{vap} \quad (2.25)$$

$H_{flow,feed}$, $H_{flow,drain}$ and $H_{flow,port}$ [W] are the heat flows associated with the mass transports in and out of the volume and Q_{ext} [W] is the heat energy provided via an external heat connector. The heat flow between the liquid and gas phase is called the water energy balance and consists of the difference between Q_{flow} and $m_{flow,water} \cdot h_{vap}$.

A second balance equation describes the mass flow balance of the gas:

$$dMX = MX_{flow,feed} - MX_{flow,drain} - MX_{flow,port} + m_{flow,water} \quad (2.26)$$

where $MX_{flow,feed}$, $MX_{flow,drain}$ and $MX_{flow,port}$ [kg/s] are the mass transports into and out of the volume and $m_{flow,water}$ [kg/s] is the evaporation rate of liquid water.

The principle of the system is illustrated by another series of equations. M_{liq} [kg] is the quantity of liquid water in the liquid phase of the system. The derivate for M_{liq} is equal to the water flow rate of the evaporation, $m_{flow,water}$ [kg/s], with reversed sign. This implies of course also inversely, that when water condensates, the mass of liquid water increases.

$$(M_{liq})' = -m_{flow,water} \quad (2.27)$$

In the dynamic equation for water evaporation below, the mass fraction of liquid water carried by the gas, X_{liq}, is driven towards the liquid mass fraction $M_{liq}/(M_{liq} + M)$, were M represents the mass of the gas in the volume. The mathematical model is given as a system in equilibrium, where water is removed successively according to a time constant, τ_{sat} [s].

$$\tau_{sat} \cdot (m_{flow,water})' + m_{flow,water} = m_{flow,feed} \cdot \left(\frac{M_{liq}}{M_{liq} + M} - X_{liq} \right) \quad (2.28)$$

The sensible heat flow, Q_{flow} [W], which is the heat flow from gas to water, is given as:

$$Q_{flow} = Akc_{water} \cdot (T_{gas} - T_{water}) \cdot M_{liq} \quad (2.29)$$

where Akc_{water} [W/K] is the thermal conductance between gas and water for a specific area, T_{gas} [K] is the gas temperature and T_{water} [K] is the water temperature.

The water energy balance is calculated as:

$$M_{liq} \cdot (h_{water})' + (M_{liq})' \cdot h_{water} = Q_{flow} - m_{flow,water} \cdot h_{vap} \quad (2.30)$$

This implies that the derivative of the enthalpy of water (obtained by the chain rule) is equal to the water energy balance. Here, h_{water} [W/m] is the specific enthalpy of liquid water and h_{vap} [W/m] is the specific enthalpy of saturated vapor.

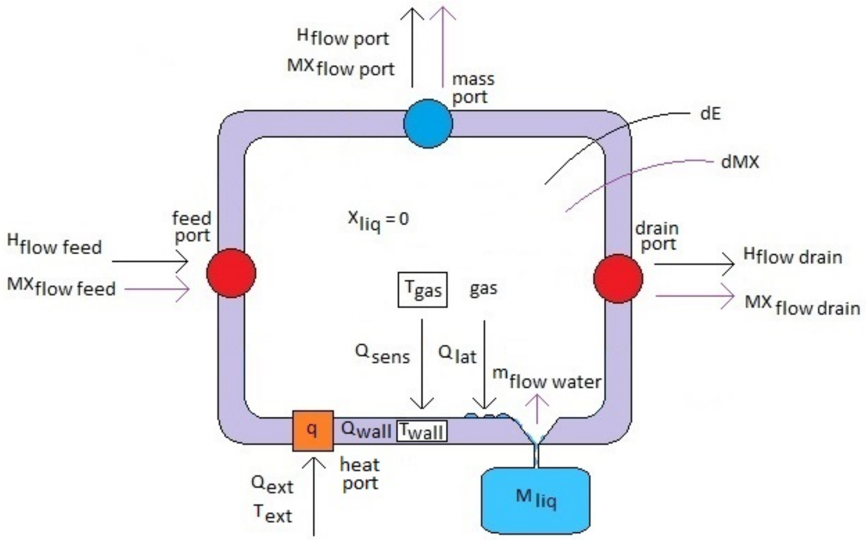

Figure 2.7 From the condensation principle model, the balance equation can be derived.

Condensation System Model The physical model is describing a condensation process which is driven by the previously mentioned concentration gradient. The system model and its principle and assumptions is explained by Figure 2.7.

Mass and enthalpy flows are transfered via the medium ports and external heat (either from the surroundings or from a specific source) can be transfered through the heat port. In this model, the external heat flow, Q_{ext}, is equal to the heat flow from the wall, Q_{wall}, and consequently the temperature of the heat port, T_{ext}, is equal to the wall temperature, T_{wall}. Two kinds of heat flows transfer energy from the gas to the water, which condenses at the wall: the sensible heat flow, Q_{sens}, and the latent heat flow, Q_{lat}. Together, they form Q_{wall}.

Just like in the separation process (Figure 2.6), the water flow is still defined in the direction from the water to the gas phase, i.e. as evaporation. Since condensed water in the gas is immediately transfered to the liquid phase, the liquid water fraction of the gas, X_{liq}, is always zero. Ideal mixing of the fluid in the volume is assumed. The condensed water has negligible volume compared to the gas. To achieve this, condensed water is immediately removed and the accumulated mass is tracked by M_{liq}. By this, the condensation becomes irreversible.

Finally, the two balance equations for this model can be derived. The energy flow balance becomes:

$$dE = H_{flow,feed} - H_{flow,drain} - H_{flow,port} + Q_{wall} \tag{2.31}$$

This equation is analogous to the energy balance equation in the separator model, with the exception that the water energy balance is omitted, since it is not applicable in this model, due to immediate leave of the condensed water.

The mass flow balance of the gas is exactly the same as in the separator model:

$$dMX = MX_{flow,feed} - MX_{flow,drain} - MX_{flow,port} + m_{flow,water} \tag{2.32}$$

For a full explanation of the model, further equations describing the physics are required. Firstly, the mass transfer coefficient, β [m/s], is derived from the heat-and-mass transfer analogy, Equation 2.33, where α [W/m^{2}K] is the heat transfer coefficient:

$$\beta = \frac{CF_{MassTransfer} \cdot 0.89^{(1/3-1)} \cdot \alpha}{Cp_{gas} \cdot \rho_{gas}} \tag{2.33}$$

In this formula, $CF_{MassTransfer}$ is a heat transfer calibration constant, Cp_{gas} [J/kg·K] is the specific heat capacity at constant pressure and ρ [kg/m^3] is the density of the gas.

The next variable is the driving gradient of the mass transfer, $d_{gradient}$, which is the driving force of the mass transfer. Condensation occurs if $d_{gradient} < 0$:

$$d_{gradient} = \frac{x_{sat,w}}{1 + x_{sat,w}} - x_{vapor} \tag{2.34}$$

In this expression, x_{vapor} is the mass fraction of vapor in the gas and $x_{sat,w}$ is the saturation water load at the wall surface, which implies the maximal fraction of vapor that can be held in the gas at the temperature of the wall. The saturation water load is calculated as

$$x_{sat,w} = k_{gas} \cdot \frac{p_{sat,state}}{p_{state} - p_{sat,state}} \tag{2.35}$$

where, k_{gas} [mol/kg] is the molar mass ratio, $p_{sat,state}$ [Pa] is the saturation pressure of the current state and p_{state} [Pa] is the pressure of the state.

Finally, the evaporation rate is calculated:

$$m_{flow,water} = \beta \cdot A_{heat} \cdot \rho_{gas} \cdot d_{gradient} \tag{2.36}$$

This expression is only valid in the interval when the $d_{gradient} < 0$, otherwise $m_{flow,water} = 0$. This is due to the fact that the model only takes condensation into account and not the reversed process, evaporation. In comparison to the separator model, this system is not always at equilibrium.

Now that the mass flow has been determined, a series of relevant heat flows will be considered. Q_{lat} is the heat flow from the condensation process

$$Q_{lat} = m_{flow,water} \cdot h_{vap,T_{wall}} \tag{2.37}$$

where $h_{vap,Twall}$ $[W/kg]$ is the specific enthalpy of vaporization.

Q_{sens} is the heat flow from gas to water:

$$Q_{sens} = \alpha \cdot A_{heat} \cdot (T_{wall} - T_{gas}) \tag{2.38}$$

The heat flow of the wall is the sum of Q_{lat} and Q_{sens}:

$$Q_{wall} = Q_{lat} + Q_{sens} \tag{2.39}$$

2.5 Stack Cooling System

In this section, the implementation of the stack cooling system, including a controller, will be described.

Principle

The cooling system of the stack is necessary to maintain the stack temperature at the desired operating point. For that purpose, a cooling medium will be pumped into the stack to absorb heat and then be cooled by an external medium outside of the stack in order to keep a closed cooling loop. Water is used as the cooling medium, which is air-cooled before going back into the loop. The most essential components of the cooling system are a set of cooling channels integrated in the stack flow field plates and external heat exchanger, where the heat of the water is transfered to the surrounding air. A pump controls the water flow rate based on the stack temperature, thereby regulating the cooling process.

The heat exchanger, which corresponds to the radiator of a car, can also be coupled with a radiator fan, to draw cooling air through the cooling flanges. For simplicity, this component is omitted and sufficient air flow is instead assumed.

Implementation

For simulation purposes, the basic parts of the cooling system (shown in Figure 2.8) consist of a pipe component incorporated in the stack component, with an active area in connection with the stack for heat transfer. A water-gas heat exchanger component represents the air cooled radiator block at the front of the car under the bonnet, where the water is cooled by the air coming in through the grill.

In order to circulate the cooling water, a pump is used. The pump must always have a positive flow, but its rotation speed will vary according to the flow rate. In order to adapt the flow to control the stack temperature, a PID controller, comparing the actual stack temperature with a reference temperature will be required.

Since the pressure in a temperature variating, closed system would reach remarkably high pressure variations, a buffer component is required. This component is composed by a multi-port volume, connecting the heat exchanger with the pump but also with a friction component. The friction component handles the pressure

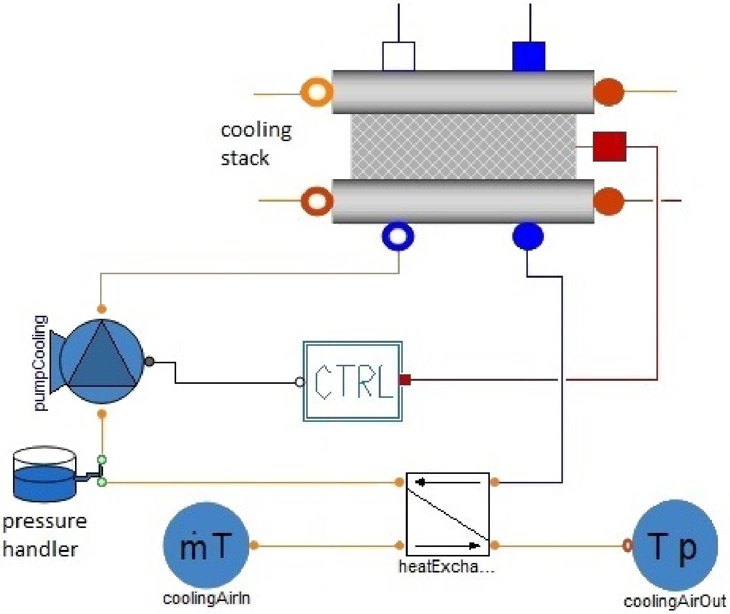

Figure 2.8 The stack cooling system consists of a pipe system inside the stack, a heat exchanger, a pump, a pressure handler component and a controller.

drop between this connector volume and a second volume, represented by an ideal, infinite sink component with a determined pressure. When the pressure of the system increases above the set sink pressure, a fraction of the liquid will be transfered to the sink. On the contrary, when the system pressure decreases, liquid from the sink will be transfered to the cooling system. This principle means the cooling system is an open system, but it behaves analogous to a buffer tank, partly filled with air, which can be compressed or expanded according to requirements. The pressure handler component is illustrated in Figure 2.9.

The control system for the pump was implemented as shown in Figure 2.10. A measured temperature signal from the stack is compared with the desired stack reference temperature, a tunable parameter that can be adjusted in the stack system code. Since a pump rotational speed in Modelica must always be larger than zero, the control signal from the PID controller is added to a small, positive value before conversion into a motor speed signal. For improved overview, the control system was merged in a cooling control component.

The different components were adjusted in individual component tests and then added one by one to the existing stack model while the pump speed was set to a steady state value. Finally, the controller was implemented. A particular auto-tuner component [Björk and Levenhammar, 2017] were used to derive the control param-

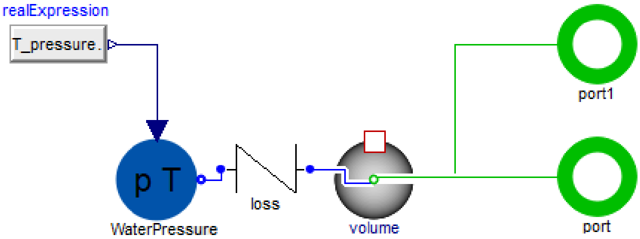

Figure 2.9 The pressure handler component consists of two volume components with a friction component in-between. The temperature of the water pressure sink can be set to follow the temperature of the liquid of the external system.

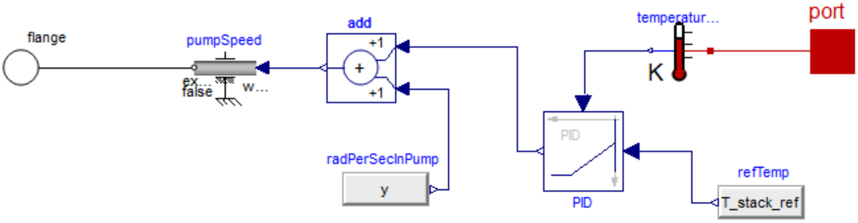

Figure 2.10 The inside of the cooling system control component. The control signal from the PID controller is added to a small positive number, *y*, before conversion into a pump signal.

eters. However, when tested, this controller did not perform well at temperatures above 90°C. Instead, the Ziegler-Nichols method [Ziegler and Nichols, 1942] was used to retrieve control parameters, this time with a more satisfactory result.

Parameterization

The parameterization of the cooling channels of the stack was performed according to an estimation of appropriate dimensions. It was assumed that each flow field plate between the MEAs had 8 parallel channels. As mentioned earlier, the number of fuel cells in the Mirai stack is 370. A fuel cell, and consequently a flow field plate, is estimated to measures 0.32×0.25 m^2 (based on the assumption of the fuel cell area being $800 \cdot 10^4$ m^2). The cooling channels are assumed to be sinus shaped to increase the active cooling area. From this, the parameters in Table 2.5 were determined.

The parameterizations of the PID controller are listed in Table 2.6.

The parameterization of the radiator was performed according to an estimation of appropriate dimensions based on Internet pictures of general car radiators. The

Parameter	***Formula***	***Value***
Number of cooling channels, n	–	$370 \cdot 8$
Channel length, L [m]	–	0.4
Channel hydraulic diameter, D [m]	–	0.0013
System volume, V [L]	$V = n \cdot A \cdot L$	1.6
Total heat transfer area, A_{tot} [m^2]	$A_{tot} = n \cdot \pi \cdot D \cdot L$	4.8

Table 2.5 Parameterization of the cooling pipe dimensions.

Parameter	***Auto-tuner***	***Ziegler-Nichols***
Ultimate gain, K_u	n.a	-2000
Oscillation period, T_u [s]	n.a	3.6
Proportional gain, P	-683	-1200
Integral term, T_i	17	1.8
Derivative term, T_d	1.06	0.45
Upper limit of output, u_{max}	3120	3120
Lower limit of output, u_{min}	0	0

Table 2.6 Parameters of the PID derived by the auto-tuner and the Ziegler-Nichols method.

model that was first derived, turned out to be insufficient at the most extreme conditions for which the final stack system was to be verified. For that reason, a model with a larger heat transfer area was parameterized in order to handle simulation at a stack temperature of 60°C and a current of 400 A withdrawn, which requires extremely efficient cooling. For most simulation runs, the first, more realistic model is recommended. Table 2.7 displays the parameterization of the two heat exchangers.

Parameter	***Heat Exchanger 1***	***Heat Exchanger 2***
Radiator dimensions $(h \times w \times d)$ [m^3]	$0.4 \times 0.5 \times 0.07$	$0.6 \times 0.6 \times 0.07$
Single channel dimensions $(l \times w \times t)$ (both water and air channels) [m^3]	$0.5 \times 0.07 \times 0.001$	$0.6 \times 0.07 \times 0.001$
Number of channels	200	300
Channel length [m]	0.5	0.6
Hydraulic diameter [m]	$2 \cdot 10^{-3}$	$2 \cdot 10^{-3}$
Cross section area [m^2]	$7 \cdot 10^{-5}$	$7 \cdot 10^{-5}$
Heat exchange area, single channel [m^2]	0.07	0.084
Water volume of radiator [L]	7	12.6
Air flow [kg/s]	2	5
Heat exchanger configuration	counter flow	counter flow

Table 2.7 Parameters of the heat exchangers.

The temperature of the pressure handler component was set to be the same as the outflow temperate of the heat exchanger water.

2.6 Humidifier System

This chapter describes the construction of the humidifier and how it was implemented and controlled.

Principle

As mentioned earlier, a controlled humidification of the PEM fuel cell membrane is essential for optimal efficiency of the power generation. Two main classes of humidifiers exist; external, where the humidifier is physically located outside of the stack and internal, where the humidifier functions are integrated in the stack.

External humidifiers can be based on a large variety of principles [Larmine and Dicks, 2003]. The currently most frequent method builds on a principle where inlet air from the compressor and outlet air from the stack are lead into each side of a device, according to a counter flow principle, where the flows are separated by a water permeable membrane. The membrane possesses similar qualities as the water transport membrane implemented earlier. Water from the exhaust air will condense on the membrane surface and diffuse through the membrane wall to humidify the air on the other side [Solsona et al., 2001] [Chen et al., 2008] [Chen and Peng, 2005].

Due to time limitations, a simpler humidifier model was desired and another principle was chosen for implementation. Water is injected into a mix chamber, in which ideal mixing and thermodynamic equilibrium is assumed, and where the liquid water is transfered to the gas and carried into the stack [Jung et al., 2007]. The humidifier also collects the water from the exhaust air and stores it prior to a controlled injection into the mixing chamber.

Once implemented in the stack system, the humidifier will be controlled by a PID controller.

Implementation

The mixing chamber was the central unit of the humidifier and would successively be extended by different components to achieve all the necessary functions for the complete humidifier system. As a starting component, available components from the FCL were considered.

- A *Condensing Volume* component, that was used as flow field channels in the stack model. Instead of removing water through the mass port, water would be injected and condensed. The condensing volume component, however, did not take into account the enthalpy (i.e. the temperature) of the incoming water, since it was not developed for this kind of application and could therefore not be used.

- A similar component, a *Condensing Steam Mix*, was instead evaluated. This model turned out to mainly be aimed for hot temperature applications and contained a lot of code for handling overheated water, which was suspected to induce an unanticipated enthalpy behavior.

- In a simplified version of the previous component, a *Condensing Water Mix* component, the high temperature behavior equations were removed. Anyhow, the enthalpy was still behaving in an unexpected way, giving a huge temperature drop to the gas. The condensing medium model used was evaluated to verify if the reference temperature of the enthalpies were equal for pure water and vapor or liquid water in a gas phase. (Since enthalpy is a *relative* measure of heat energy, a reference temperature when defining it to zero is chosen. For most media models, it is chosen to 25°C, but for some, it is defined at 0°C.) Some adjustments of reference enthalpies were made, but still a temperature drop of the gas was received.

- *Simple Water Mix* This component possessed ideal mixing and gave an instant equilibrium with a steady state value as output. In order to create a very simple mixer component, only boundary conditions of mass and energy balances were taken into account, thereby omitting equilibriums inside of the component. Since the gradient determining the evaporation, $\left(\frac{M_{liq}}{M_{liq}+M} - X_{liq}\right)$ introduced in Equation 2.28, was also removed, the steady state response would be slightly different. Still, the simplified component brought a temperature drop to the gas.

The temperature drop in the components was found to occur due to a physical phenomena called the *wet bulb temperature effect*. The wet bulb temperature is the temperature that the air would have if it were cooled to its saturation temperature (i.e 100% relative humidity) by the evaporation of water into it [Dunlop, S., 2008]. This implies the wet bulb temperature is the lowest temperature that can be reached under current ambient conditions by the evaporation of water solely. It is therefore dependent of the ambient air temperature and the humidity [Kroos, K. A., 2016].

In the mixer chamber, liquid water enters and evaporates into the warm air. Heat taken from the air is used for the evaporation, while bringing the air to saturation. Since we assume ideal mixing in the chamber, the air will also carry the rest of the water as liquid water particles, expressed by the earlier introduced variable, X_{liq}. In order to counteract the temperature drop and to preheat the air prior to transferring it onto the stack, a method described in literature [Jung et al., 2007] to warm the chamber by the outgoing cooling water from the stack was to be applied. The humidifier structure is introduced in Figure 2.11.

The heating part, on top of the system, is implemented as a pipe component, parameterized as a channel system surrounding the chamber with a heat transfer area. A heat connector transfers heat to the mixing chamber (called *simple mixer* in Fig-

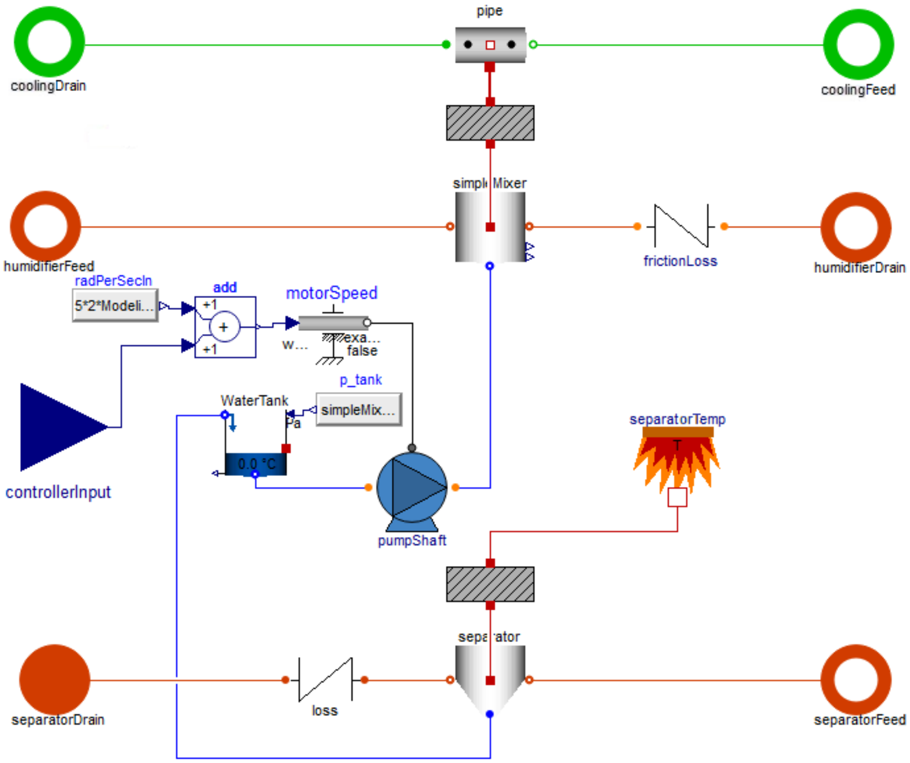

Figure 2.11 The humidifier component has seven connectors and comprises the three functions water separation, air humidification and chamber warming.

ure 2.11) via a steel wall, parameterized by wall thickness and material properties of steel.

In the chamber, compressed air enters and exits through the flow ports and is mixed with water injected through the mass port at the bottom.

The exhaust air enters the separator, in which water is taken out according to the same kind of equilibrium principles as given in Equation 2.28. The water separated is passed on through the mass port and the dried air exits though the second flow port. The separator is heated by a fixed temperature heat source connected to a steel wall, modeling the separator volume wall. The water separation in the volume is dependent on the temperature difference between the warm exhaust air and the cooler separator temperature.

The condensed water is stored in a water tank, which is a modified version of an available *Open Water Volume* component from the FCL. The component has been modified in two ways. Firstly, the excess water will spill out when the volume becomes overfull and secondly, the pressure in the tank will be constant and not dependent on the height of the water level. By this, a simpler and more predictable system is received.

To avoid fluctuations in the pressure difference between the pump inflow and outflow, which will make the pump implementation much more difficult, the water tank pressure is set to follow the mixer chamber pressure.

Since the pump flow in Modelica must always be positive, a small positive rotation number is set to default and added to the external control input signal of the rotation speed of the pump.

The humidifier interacts with its surroundings via seven different connectors. Two flow ports handle the cooling water flow, which enters the component from the stack and proceeds to the heat exchanger for cooling. Another two flow ports handle the hot air, which has been compressed and proceeds into the stack after humidification. A final pair of flow ports transfer exhaust air from the cathode side of the stack to the separator and the dried air continues through the exit port to a sink boundary, representing the ambient atmosphere.

The humidifier also contains two friction loss components. These kind of components are used when modeling pipes, since pipe models always must contain volumes and friction alternating to model the system correctly and avoid unnecessary non-linear systems.

In the humidifier parameter menu, there is a boolean function for enabling or disabling the cooling water heating function, where the default setting is enabled. In terms of coding, if the boolean equals true, there is a heat connector between the mixer chamber and the steel wall and it the boolean equals false, there is no connector and thereby no heat transfer.

After implementation and testing of the humidifier on the cathode side of the stack, as displayed in Figure 2.12, a PID controller was connected to keep the humidity of the air on the cathode side of the stack at a reference value. Unfortunately, the auto-tuner was not compatible with the kind of system formed by the humidifier and since no oscillation of the control signal could be produced, the system had to be manually tuned.

Parameterization

The parameterization of the pipe channels warming the mixer chamber was performed according to an estimation of the appropriate dimensions. The pipe system was assumed to have 10 parallel cooling channels surrounding the chamber and the channels were assumed to be serpentine shaped to increase the active cooling area. Based on these assumptions, the parameters in Table 2.8 were determined.

The initial temperatures of the pipe system, the mixer chamber and the separator were set to $(T_{stack} - 5)$°C and the variable heat source temperature of the separator cooler was set equal to the ambient temperature.

The parameterization of the PID controller is listed in Table 2.9.

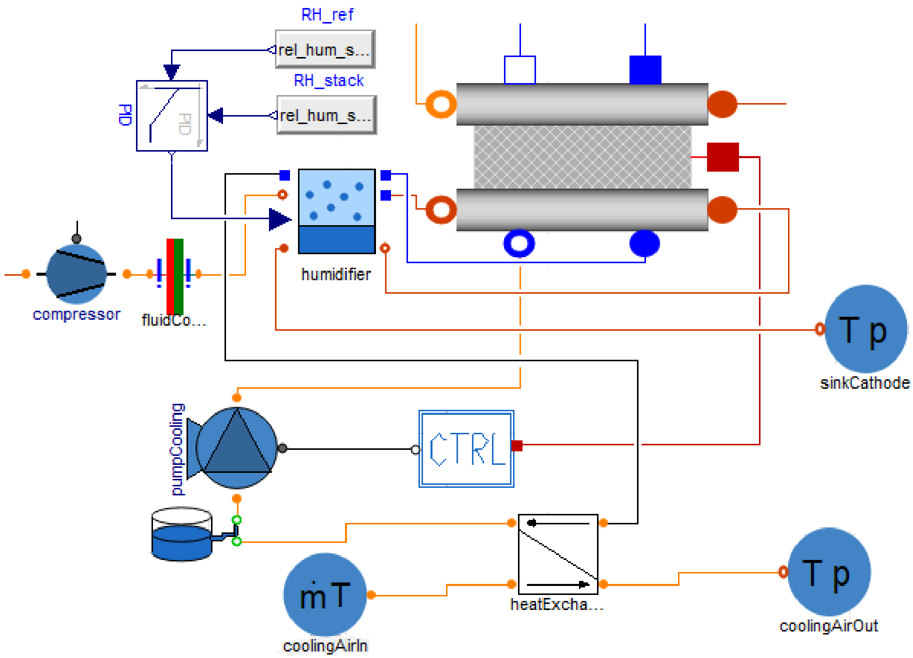

Figure 2.12 The humidifier component is the spider in the web, connecting the compressor to the stack, the outgoing stack cooling water to the heat exchanger and the cathode outlet to the sink. Finally, the PID controller is plugged in.

Parameter	*Value*
Number of cooling channels, n	10
Channel length, L [m]	3
Channel hydraulic diameter, D [m]	0.01
Cross section area A_{cross} [m^2]	$7.85 \cdot 10^{-5}$
Total active area, A_{heat} [m^2]	0.5

Table 2.8 Parameterization of the humidifier pipe system.

2.7 Fuel and Air Supply

In this section, a robustness improvement in the anode loop and the control implementation of the air and fuel supply are discussed.

Principle

In a stack system, required to provide different power at different instants and where the demands change rapidly, the provision of control of fuel and air supply are

Parameter	***Value***
Relative humidity stack, ref. value	0.9
Proportional gain, P	6000
Integral term, T_i	9
Derivative term, T_d	0.5
Upper limit of output, u_{max}	350
Lower limit of output, u_{min}	0

Table 2.9 Parameters of the PID controller of the humidifier.

mandatory.

On the anode side of the stack, the hydrogen flow will be equipped by an improved control system and on the cathode side, the compressor rotation speed will be controlled in order to adjust the cathode pressure and thereby the amount of oxygen supplied to the system.

Implementation

Anode Side When starting evaluating the earlier constructed anode loop, the stack system was found to be non-robust, since the simple system version of the loop was not implemented according to the principle of alternating volumes and friction loss components (earlier mentioned in Section 2.6). A first modification was therefore to add one friction loss component and two volume components, of which one was a three way joint in the anode loop. The implementation is shown in Figure 2.13 and can be compared to the earlier version of the simple stack system (Figure 2.4).

Further, the simple stack implementation of the P-controller of the valve was also found to be incorrect. The fuel mass flow parameter implemented, m_{fuel}, did not correspond to the flow in the loop, and was actually significantly smaller, although still sufficiently large, to provide the stack system with hydrogen. The valve was controlled according to the difference between m_{fuel} and the outgoing flow of the stack, instead of correctly, the substantially smaller difference between the incoming and outgoing flow of the stack. This resulted in a too large valve opening.

When the anode loop was rebuilt to control the valve opening degree according to the true hydrogen consumption, an initialization problem was received. This was due to that the initial difference between inflow and outflow of the stack was zero, which lead to a zero opening of the valve. This implied that hydrogen to be consumed could never start entering the loop. However, this could be resolved by setting a small minimum flow to the valve, but the solution was not ideal, since hydrogen would then be injected into the loop also when no current was drawn from the stack.

Another attempt was to try regulating either the valve or the hydrogen source component directly according to the cathode stoichiometry, which is the ratio of total oxygen flowing through the cathode and the oxygen consumed. Due to huge variations in stoichiometry, this was however found to give a really aggressive response when connected to a gain component (magnifying the signal by a proportional factor). When trying to adjust this, the proportional gain had to be lowered to a level where it basically had no effect. No trials of low pass filtering the signal were performed.

Instead, when evaluating the loop system further, the flow of the loop was found not to be affected as long as the valve was at least about 10% open. The reason for this was that the system was pressure controlled and not flow controlled, although the valve was adjusted according to a flow.

As long as the valve did not choke the flow, the anode system was found to always keep the assigned pressure of the hydrogen source component also in the loop. This pressure simply corresponded to the lower flow earlier observed in the loop. During operation, the amount corresponding to the hydrogen consumed by the stack would be let in through the valve, and this was controlled by keeping the pressure constant. The overall conclusion from this, was that the valve function was unnecessary, since the loop was self-regulating by the pressure. The valve was removed and since it was a friction regulating component, it was substituted by another friction loss component. The final anode loop system is displayed in Figure 2.13.

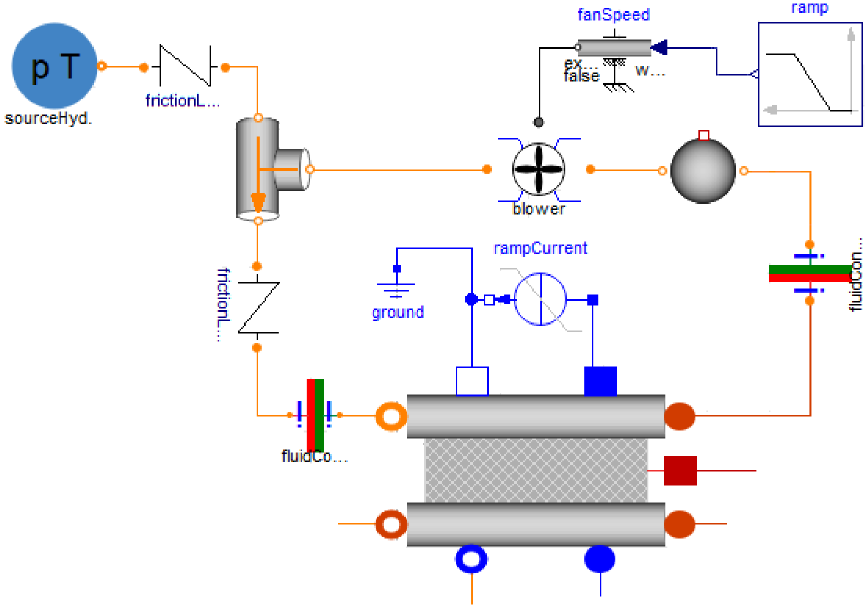

Figure 2.13 The anode loop contained volume components and friction components alternating.

Cathode Side At the cathode side, the compressor rotational speed could be controlled in three different ways. The control signal could either be a function of the current drawn from the stack, of the partial oxygen pressure at the exit of the stack or of the hydrogen consumption at the anode.

It appeared rational to direct one electrode flow according to another, since the demand of oxygen was strictly proportional to the hydrogen consumption, and the hydrogen consumption, in its turn, was proportional to the current withdrawn. The compressor control system is displayed in Figure 2.14.

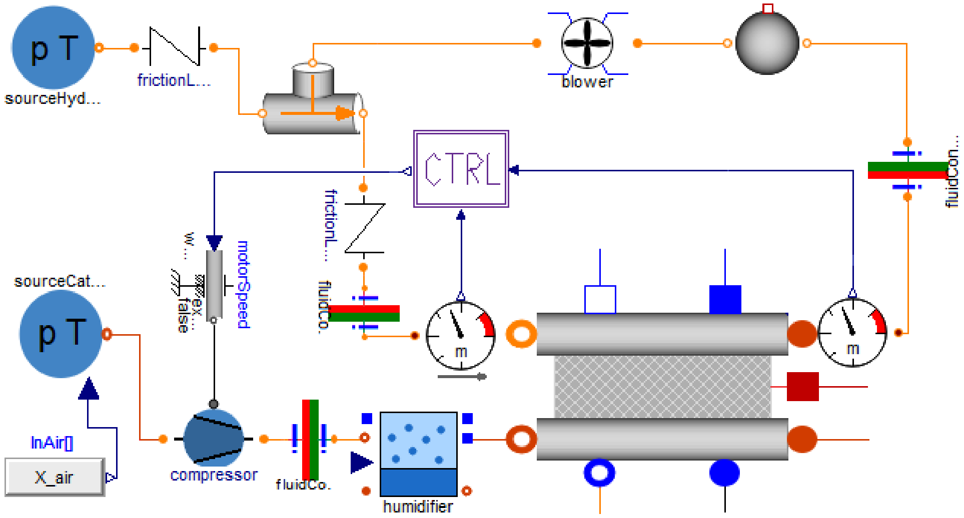

Figure 2.14 The control system of the compressor forms a connection between the anodic and the cathodic parts of the system.

When evaluating the behavior of different cathode pressures in the potential operation interval, 2.1-2.9 bar, the humidifier pump was found to get negative flows at higher compressor induced pressure, since the pressure on the feed side of the pump became a lot lower than on the drain side. Negative flows in pumps are not applicable in a real system and neither allowed in Modelica and thereby interrupted the simulations. This was resolved by coding the pressure of the humidifier water tank to follow the pressure of the stack on the cathode side, as earlier described in the humidifier implementation chapter, Section 2.6.

The stack system was mapped by examining its behavior at various anodic and cathodic pressures, currents and cell areas. From this data, the compressor rotational speed was determined to optimize the system in terms of cell voltage, cathode flow, cathode stoichiometry and efficiency. Since the compressor is by far the most power consuming auxiliary device in the stack system, the pressure should not be higher than necessary, but at the same time provide a sufficient cathode stoichiometry. According to literature [Larmine and Dicks, 2003], a cathode stoichiometry around 2 is typical and it should not fall below 1.75. A higher air flow increases the partial pressure of oxygen, pO_2. This, in its turn, increases the cell voltage according to the Nernst equation, Equation 1.1, in the introduction chapter. The increase in cell voltage must be traded of against the increased power consumption of the compressor.

As mentioned, the hydrogen consumption will control the rotational speed, the cathode pressure and the oxygen supply, but inversely, these activities on the cathode side of the stack will not affect the hydrogen consumption (as long as we have an excess of oxygen). For that reason, an open loop regulation and not a feedback control system was obtained. Hence, a PID controller could not be used. Instead, the regulation would be performed according to a linear equation of the form

$$y = k \cdot x + m \tag{2.40}$$

where x is the hydrogen consumption, y is the rotational speed of the compressor, k is the proportionality constant and m is the rotational speed when the stack is idle.

Since the system was sensitive to negative flows and also noisy during initialization, a series of *min* and *max* blocks were used when implementing the control system. The blocks filtered negative flows out, but also ensured that the theoretical max flow in the loop could not be exceeded and that the hydrogen consumption always had non-negative values. The control logic in Figure 2.15 was encapsulated in a control component.

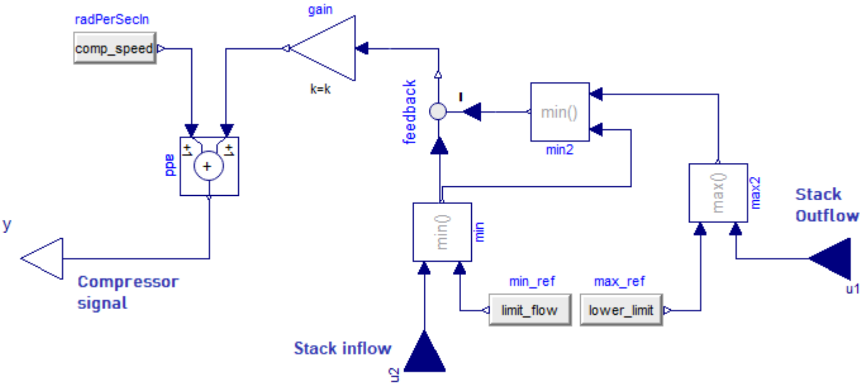

Figure 2.15 The compressor control system logic to process the stack flow signals. The parameter *comp_speed* corresponds to m and the gain to k in Equation 2.40.

Parameterization

Anode Side The absolute pressure of the anode system was set to 2.0 bar in order to increase the mass flow of the loop and thereby also both the consumption margin and the anode stoichiometry.

Cathode Side From the mapping of the stack system behavior, four operation points of satisfactory efficiency in the desired pressure interval were chosen to represent the system behavior. The system is mainly intended for use in the current interval 250-450 A and the cathode pressure interval 2.1 - 2.5 bar. The data of these points is given in Table 2.10.

Current	***250 A***	***350 A***	***400 A***	***450 A***
Cathode pressure [bar]	2.14	2.41	2.51	2.62
Cell voltage [V]	0.90	0.83	0.78	0.71
Stack power [kW]	0.83	1.07	1.16	1.19
Compressor speed [$\times 2\pi/60$ rad/s]	2100	2450	2600	2800
Compressor flow [kg/s]	0.062	0.088	0.098	0.109
Hydrogen consumption [g/s]	0.97	1.35	1.55	1.74
Cathode stoichiometry	1.87	1.89	1.84	1.83
Anode stoichiometry	2.48	2.05	1.92	1.82
Percent of generated stack power consumed by aux. device [%]	9	11	12	14

Table 2.10 The four operating points (steady state values) chosen to represent the system behavior and from which a linear equation was extrapolated. The cell area and the anode pressure were constant: $A_{cell} = 800 \cdot 10^{-4}$ m^2 and p_{anode} = 2.0 bar.

The rotational speed of the compressor was plotted as a function of the hydrogen consumption. The coefficients k and m were determined by linear regression. The *limit_flow* parameter in Figure 2.15 was set to the maximum possible anode loop flow at 2.0 bar. The parameterization of the control logic is given in Table 2.11.

Parameter	***Value***
k [$\times 2\pi/60$ rad/kg]	93806
m [$\times 2\pi/60$ rad/s]	1230 (=128.8 rad/s)
$limit\_flow$ [kg/s]	0.00318
$lower\_limit$ [kg/s]	0

Table 2.11 Parameters of the control logic of the compressor.

2.8 Flow Machines

In this part of the project, efficiency tables determining the power consumption of the compressor, the anodic blower and the two pumps in the cooling system and the humidifier were to be implemented.

Principle

In Modelica, non-ideal flow directing components are equipped with two types of tables to determine their behavior in terms of volumetric flow and power consumption.

The task of a flow machine is to relate the pressure difference between its upstream and downstream sides to the output flow rate and the resulting power consumption. In order for the components to respond to an input rotational speed, the flow tables must be implemented for the interval considered. This was performed once the components were inserted in the models earlier during the project.

To have Modelica calculate the power consumption, also the power tables must be implemented.

For the compressor, the first type of table handles the effect on the flow as a function of rotational speed and pressure ratio between the downstream and upstream sides. Each combination of speed and pressure in the table matrix corresponds to a volume flow. The volume flows for the different values can be plotted as curves in a *flow map*.

In the same way, *efficiency maps* can be plotted from tables stating the efficiency at different rotational speeds and pressures. The efficiency maps are used for the power consumption calculation.

For pumps and fans, the principles are slightly simpler. The flow table only consists of a series of operation points mapping a specific pressure change across the component (i.e. the resistance to master) to a certain flow. From this, a curve connecting the points can be plotted.

In the same way, a mapping of power consumption to overcome different pressure changes can be implemented, to plot a relationship thereof.

General plots of the curve types described are displayed in Figure 2.16.

Implementation

Based on literature [Larmine and Dicks, 2003], [Pumpportalen, 2015], [The engineering tool box, 2017a], [The engineering tool box, 2017c], power consumptions of the compressor, the pumps and the fan were estimated at the different operation points. The implementations were chosen as simple as possible and the power values were estimated based on similar fluid systems.

The theoretical power of the compressor, P_t [W], is proportional to the temperature increase, the rate of flow of the gas and the specific heat capacity of the gas.

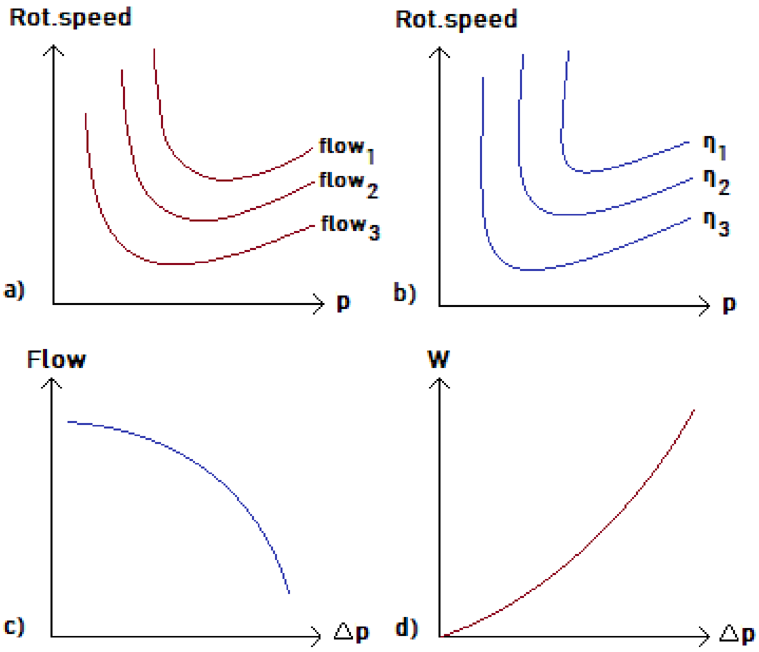

Figure 2.16 a) Compressor flow map b) Compressor efficiency map c) Pump or fan flow curve d) Pump or fan power curve.

From literature [Larmine and Dicks, 2003], the expression

$$P_t = c_p \cdot \frac{T_1}{\eta_c}\left(\left(\frac{p_2}{p_1}\right)^{\frac{\gamma-1}{\gamma}} - 1\right) \cdot m_{flow} \tag{2.41}$$

is obtained. Here, c_p is the specific heat capacity of air (c_p = 1004 J/(kg·K)), T_1 [K] the temperature of the incoming air, η_c the isentropic efficiency derived from the compressor efficiency map, $\frac{p_2}{p_1}$ the pressure ratio between downstream and upstream, γ a gas law coefficient ($\gamma = 1.4$ at 293 K) and m_{flow} [kg/s] the mass flow. The theoretical power require further adjustments for mechanical losses in the bearings and the drive shafts, as well as for electrical losses in the motor [Larmine and Dicks, 2003].

The ideal, hydraulic pump power, P_h [W], is

$$P_h = \frac{q \cdot \rho \cdot g \cdot h}{3600} \tag{2.42}$$

where q [m^3/h] is the flow capacity, ρ [kg/m^3] the fluid density, g the gravity constant (g = 9.81 m/s^2) and h [m] the differential head. The differential head is the pressure increase recalculated into the metrical height of a liquid column of the fluid corresponding to the pressure. 3600 [s/h] is a conversion factor.

Taking losses into consideration, the total power, P_{pump} [W], is

$$P_{pump} = \frac{P_h}{\eta_p \cdot \eta_m} \tag{2.43}$$

where η_p is the efficiency of the pump and η_m is the efficiency of the motor [Pumpportalen, 2015], [The engineering tool box, 2017c].

The ideal, physical fan power consumption, for just performing the work, is calculated according to

$$P_i = \Delta p \cdot q \tag{2.44}$$

where P_i [W] is the ideal power consumption, Δp [Pa] the total pressure increase and q [m^3/s] the air volume flow delivered by the fan. Efficiency is taken into regard according to

$$P_{fan} = P_i / \eta_f \tag{2.45}$$

where P_{fan} [W] is the total power used and η_f is the fan efficiency [The engineering tool box, 2017a].

From the formulas above, power consumption values in the intended operation ranges were calculated and the tables were constructed accordingly.

Finally, a calculation of the stack system power efficiency was implemented in the code.

$$\eta_P = \frac{P_{stack} - P_{comp} - P_{coolpump} - P_{fan} - P_{humipump}}{P_{stack}} \cdot \eta_{cell} \tag{2.46}$$

The first part of the expression considers the power consumption used by the auxiliary devices. The second part, η_{cell}, takes the losses during the electricity generation in the fuel cell into account. η_{cell} is calculated as

$$\eta_{cell} = \frac{P_{cell}}{P_{cell} + Q_{cell}} \tag{2.47}$$

where P_{cell} [W] is the useful power of the fuel cell and Q_{cell} [W] is the heat development of the fuel cell.

By this, the final version of the stack system was completed and is displayed in Figure 2.17.

Parameterization

The parameterization intervals implemented in the tables are given in Table 2.12. When estimating the pump heads, a pressure increase of 0.5 bar was assumed. This corresponded to a 5.1 m water pillar. The ideal power consumptions were divided by numerical values of assumed efficiency coefficients.

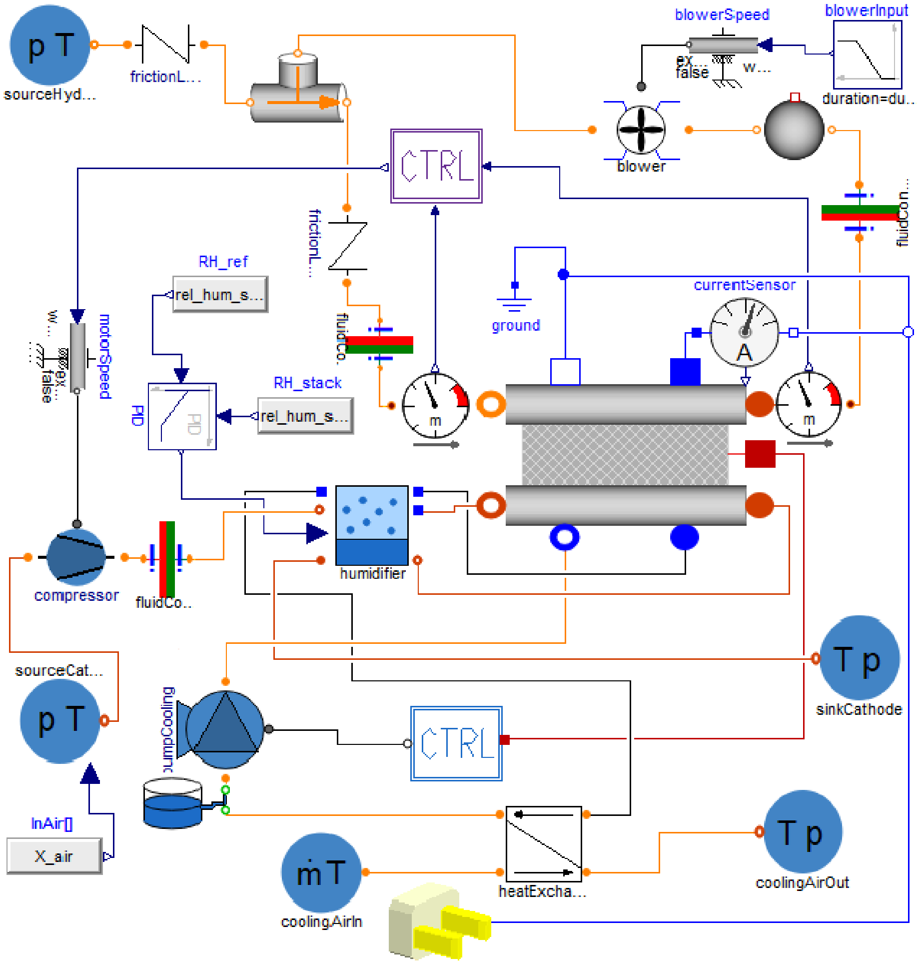

Figure 2.17 The final stack system with humidifier, cooling system and controllers implemented.

2.9 Current Control Logic

As a last part of the development process, the final stack system would be connected to the template in order to run the full FCHV system. The *dcdcController* sub-model inside of the controller module of the template (see Figure 1.1) first required some additional functions, in order to direct the current of the stack according to the demands of the motor. To achieve this, a few stack parameters associated with the stack power had to be determined.

Device	***Flow***	***Interval***	***Power***	***Interval***
Compressor	p ratio	0-2.5	p ratio	1.5-3.0
	Rot. speed	1500-3000 min^{-1}	Rot. speed	0-2500 min^{-1}
Cooling pump	Nom. flow	$1 \cdot 10^{-5} - 3 \cdot 10^{-4}$ m^3/s	Nom. flow	$1 \cdot 10^{-5} - 6 \cdot 10^{-3}$ m^3/s
	Nom. head	0-5 m	Power	0.5-300 W
Humidifier pump	Nom. flow	$-1 \cdot 10^{-6} - 1.25 \cdot 10^{-5}$ m^3/s	Nom. flow	$1 \cdot 10^{-6} - 2.4 \cdot 10^{-5}$ m^3/s
	Nom. head	0-5 m	Power	1-25 W
Fan	Nom. flow	0.001-0.1 m^3/s	Power	9-27 W
	p incr.	0-100 000 Pa	p incr.	0-100 000 Pa

Table 2.12 Flow and power tables. The mechanical efficiency of compressor was set to $\eta_{mech} = 0.75$.

Principle

For directing the stack current, the maximum possible current, I_{max}, must be determined. I_{max} is related to the fuel cell area, A_{cell}, and the maximum power of the stack, P_{max}. The easiest way to direct the stack current would be to program it to follow an appropriate motor signal, which can be transfered via the signal bus net, connecting all sub-models of the template. The stack current is withdrawn from the first DC/DC converter component, attended in Section 2.2. Communication between the DC/DC converter and the controller is also transferred via the signal bus.

Nevertheless, the SOC of the battery will also be taken into consideration as a decisive signal of when the stack should generate energy. Since the Toyota Mirai control algorithm is unknown, a simple algorithm will instead be implemented.

Implementation

Choosing the motor current signal to determine the stack current signal appeared natural, but since the stack and battery could not manage such aggressive signal fluctuations, the motor current signal required some filtration to decrease its derivative. Nevertheless, the motor current could be negative when the vehicle was moving forward, due to the storage of energy to the battery during deceleration. However, a negative current cannot be withdrawn from the stack. For those reasons, negative values of the motor current were limited to zero and the signal was passed through a filter component.

The interior of the *dcdcController* component is displayed in Figure 2.18. The *source* component contains the algorithm determining the stack current signal and will be attended further down in this section. This component requires two external signals affecting the stack current. The first signal is the SOC of the battery and the second signal is the motor current demand. Since the motor current must not fall below zero, a max block prevents negative values. As the motor voltage and the stack voltage are not equal, the motor current and the stack current will also have different magnitudes. For that reason, the motor current signal is multiplied by a quotient of V_{motor} and V_{stack}.

The stack current signal exiting the *source* component is filtered, in order to smoothen its slopes and is then transferred via the signal bus, illustrated by the yellow socket plug.

The *index* box indicates that the current signal corresponds to the incoming stack current, I_1, in the DC/DC converter and the voltages are communication signals in the same.

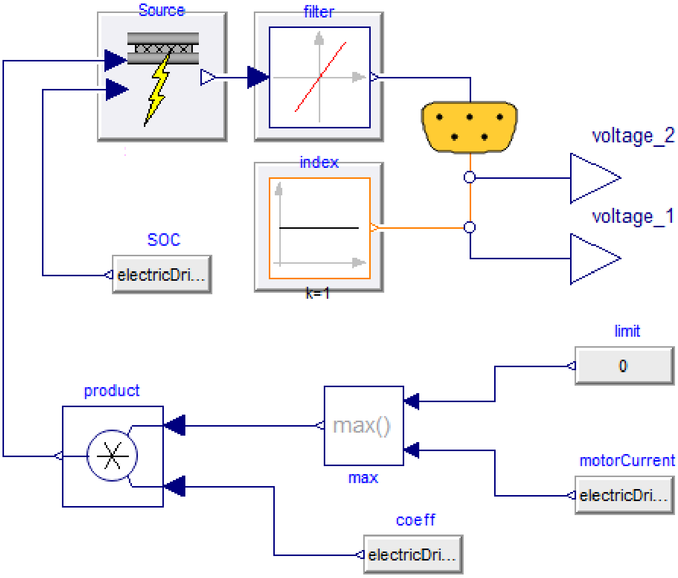

Figure 2.18 In the *dcdcController* component interior, the input signals are the motor current and the SOC of the battery. The stack current is the output signal, transferred by the signal bus.

During simulation, the algorithm inside the *source* component returns y, the current to be withdrawn from the stack, according to Figure 2.19. The system requires one second for start-up for humidification, during which the current must be zero. Thereafter, if the SOC is below a minimum value, *SOC switch*, the battery should be charged and y should be set to the highest possible I_{max}. Otherwise, if I_{cmd}, the current demanded by the motor, is equal to or higher than what the stack can deliver,

I_{max} is commanded. In all other cases, the stack should simply deliver the current demanded.

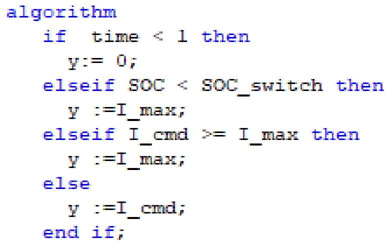

```
algorithm
   if  time < 1 then
     y:= 0;
   elseif SOC < SOC_switch then
     y :=I_max;
   elseif I_cmd >= I_max then
     y :=I_max;
   else
     y :=I_cmd;
   end if;
```

Figure 2.19 Algorithm determining the current inside the *source* component in the previous illustration, Figure 2.18.

After implementation and testing of the final full FCHV system, the model was ready for validation and drive cycle testing.

Parameterization

According to Toyota [Toyota, 2016a], the maximum stack power output for the Mirai is 1.14 kW. In order to leave some margin to losses from the water transport membrane, which should be used if its bugs were resolved, it was decided to choose P_{max} = 1.18 kW. The stack temperature considered was 70°C. The stack power is proportional to the current density i, the fuel cell area A_{cell}, and the stack voltage V_{stack}, according to the expression

$$P = i \cdot A_{cell} \cdot V_{stack} \tag{2.48}$$

where the current is given by

$$I = i \cdot A_{cell} \tag{2.49}$$

Since I_{max} is dependent of the cell area, we have to estimate A_{cell}.

According to Mirai data [Toyota, 2016a], the stack volume is 37 L and the thickness of a fuel cell is 1.34 mm. The length of the stack, consisting of 370 fuel cells, becomes

$$L_{stack} = 370 \cdot 0.00134 \text{ m} = 0.50 \text{ m} \tag{2.50}$$

This gives the cell area

$$A_{cell} = \frac{0.037}{0.50} \text{ m}^2 = 7.4 \cdot 10^{-2} \text{ m}^2 \tag{2.51}$$

As earlier shown in Figure 1.3, the cell voltage decreases as the current increases, due to increased losses. The cell voltage at I_{max} should not fall below 0.6-0.7 V, since the efficiency then will become too low. This implies that I_{max} should not be set too high, since this will decrease V_{cell}, P_{max} and $\eta_{voltage}$. In order to reach a sufficient P_{max}, the cell area had to be adjusted. The final parameterization follows in the Table 2.13.

Parameter	***Value***
P_{max} [kW]	1.18
I_{max} [A]	450
A_{cell} [m^2]	$8 \cdot 10^{-2}$
$V_{cell,min}$ [V]	0.71

Table 2.13 Parameters of the stack.

The *dcdcController* component was parameterized according to the Table 2.14.

Parameter/Variable	***Value***
SOC_{switch}	0.5
I_{max} [A]	450
$coeff$	V_{motor}/V_{stack}
k_{rising} (filter coefficient)	50

Table 2.14 Parameters and variables of the DC/DC controller.

2.10 Drive Cycle Testing

Principle

Three drive cycle tests were chosen to test the validated final full FCHV system. The drive cycle tests are briefly described below. Each cycle was simulated at three different ambient temperatures; 1°C, 25°C and 45°C in order to examine performance in different environments. Due to limitations in the water medium model used in the system model, simulation is unable to start at temperatures lower than or equal to zero.

- *US06 HWY* This 368 s drive cycle is taken from the highway part of the US06 drive cycle. This test is developed by EPA, the environmental protection agency of the United States [EPA, 2017].
- *UDDS* Urban dynamometer driving schedule, represents a 1369 s ride under city driving conditions, with lower velocities and frequent stops [EPA, 2017].
- *IM240* A dynamometer schedule developed by the EPA. This is a cycle used for inspection and maintenance which covers a 240 s ride at varying velocities [Dieselnet, 2017]. The drive cycle contains driving at medium velocities without frequent stops, like country road driving.

The velocity profiles of the drive cycles are illustrated in Figure 2.20.

Before running the drive cycle tests, the weight of the vehicle was set to 1850 kg, which is the Toyota Mirai kerb weight [Toyota, 2016c].

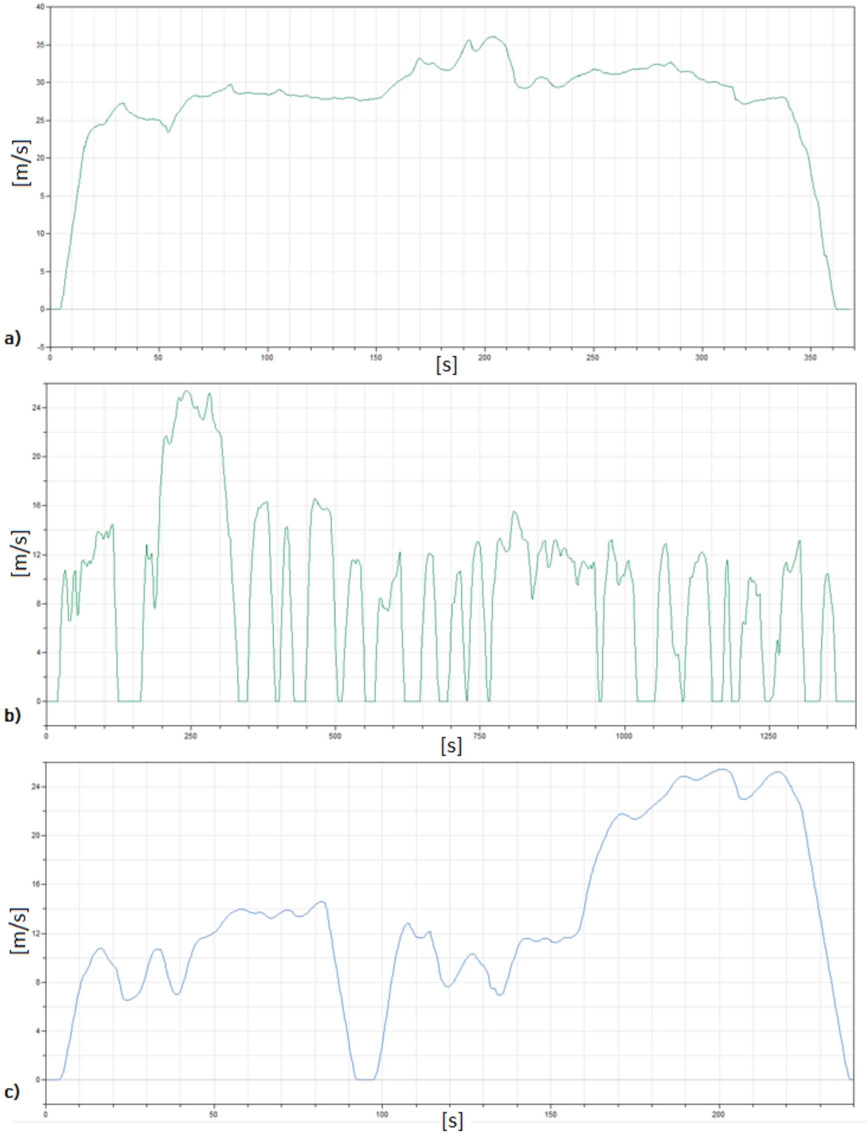

Figure 2.20 The 3 drive cycles tested; a) US06 HWY, b) UDDS, c) IM240.

3

Validation

Of the components that were developed in the project, four were validated for a more comprehensive mapping of their behavior. The components are the *Electro Chem Simple* membrane, the *Simple Water Mix* volume, the humidifier and the channel component. The final full FCHV system was also validated.

Validation plots and data are displayed in the appendices chapter. For the validations requiring a stack model, the *Electro Chem Simple* membrane was used.

3.1 Electro Chem Simple Membrane

The membrane was validated in a membrane test, by comparing it with the results of the reference *Electro Chem* membrane. The validation was performed in the ranges displayed in Table 3.1.

Variable	***Range***
Temperature [°C]	70-100
Relative humidity - air [% RH]	70-100
Relative humidity - hydrogen [% RH]	0-100
Air pressure [bar]	1.5-3.5
Hydrogen pressure [bar]	0.4-2.0*

Table 3.1 The validation intervals used for the *Electro Chem Simple* membrane. *0.4-2.0 bar is the low pressure region of the hydrogen supply [Toyota, 2016b].

The membrane was also tested in a stack test, where it was connected to anodic and cathodic condensing volume channel plates and was found to behave as expected.

3.2 Channel Component

The channel component was validated by comparing the behavior of the original *Condensing Volume* component with the implemented separator model and the *Dis-*

tributed Channel Moist Air component with the implemented condensing model. The third choice of model, where the condensation was shut off, was also checked to verify that no unexpected mass or energy exchange occurred.

The models were simulated in a 10 s test initiated at 80°C. After 4 s, a temperature reduction lasting for 2 s was introduced, to lower the temperature to 65°C. This temperature reduction induced a distinct condensation process.

3.3 Humidifier

The *Simple Water Mix* component was validated in a simple component test and the result of the temperature drop at different humidities were compared with a *psychrometric chart*. The latter is a chart showing the relationship between the wet bulb (the lowered temperature) and dry bulb (the initial temperature of the gas) temperatures and the relative humidity [The engineering tool box, 2017b].

The humidifier component was validated in a simple humidifier test, where different operation temperatures and pump speeds could be verified at steady state.

3.4 Final System

The final full FCHV system was validated by running a 100 s simple drive cycle, which had also been used for testing during the model development. The drive cycle velocity profile is illustrated in Figure 3.1. The drive cycle was simulated at stack temperatures of 60, 70, 80, 90 and 100°C and the plots of the behavior for a series of variables were evaluated.

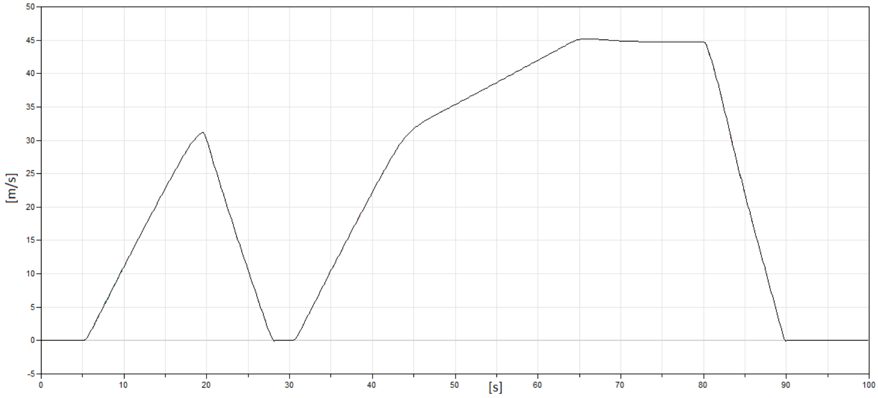

Figure 3.1 The default drive cycle used for the final system validation. The diagram displays the vehicle velocity.

4

Results

Due to the problems with the *Water Transport* membrane, system testing and validation was performed with the *Electro Chem Simple* membrane.

4.1 Simple System Model

The full simple version of the system was possible to simulate and the drive cycle test could be successfully run. However, a number of limitations were found as the system was tested. The anode feedback system of this model was found a bit non-robust, since the simulation was interrupted if the calculations went out of range and towards infinity or if the derivatives of the plots became too steep during simulation. The simulation ranges of certain parameters, for example the fan speed, were also limited. The hydrogen density in the feedback loop seemed remarkably low (about 0.1 kg/m^3), but this was found to be reasonable when controlled by hand calculations according to the ideal gas law:

$$\rho = \frac{M \cdot p}{R \cdot T} = \frac{2.02\ \frac{g}{mol} \cdot 1.5\ \text{atm}}{0.0821\ \frac{L \cdot atm}{K \cdot mol} \cdot 353\ \text{K}} = 0.105\ \text{g/L} = 0.105\ \text{kg/m}^3 \qquad (4.1)$$

Although the system was simulated with pure hydrogen fed into the anode, it was found that a constant 4% H_2O was received in the loop. This turned out to be created in the condensing medium at the initialization due to a required non-zero value for the numerical solver. This bug may be hard to come around unless a membrane possessing functions for transporting water molecules through the membrane is implemented. Anyhow, it did not imply any problems for running the system.

The power train part of the system showed a robust behavior after increasing the number of parallel cells of the battery in the full FCHV system. By this, the derivatives of the curves became less steep. However, a bug was encountered in the battery component provided from the standard library. The charge of the battery cell became close to undrainable. This was compensated for by temporarily lowering the value of the cell charge, until the bug is resolved in a future version of the library.

The full FCHV system, with the simple stack system modules implemented, was simulated with converter efficiencies, η, in the interval 0.8-1 and the model was found robust enough to handle such losses.

4.2 PEM Fuel Cell

Electro Chem Simple Membrane

Since the membrane is a new component, it was tested and validated according to the validation chapter, Section 3.1.

From the comparison of the original membrane with the simplified one, it can be stated that the membranes coincide very well except from when the operation temperature is changed from its original 80°C. Then the voltage output errors will grow with the temperature change. The temperature related voltage changes are magnified in the simpler membrane and the deviations also grow by increasing stack current, as displayed in Figure 4.1. Since the original membrane is more detailed, thereby taking more temperature dependencies into regard, this model gives a more correct output. Concerning the general membrane behavior, it was found that the output cell voltage decreases with increased temperature and the inverse.

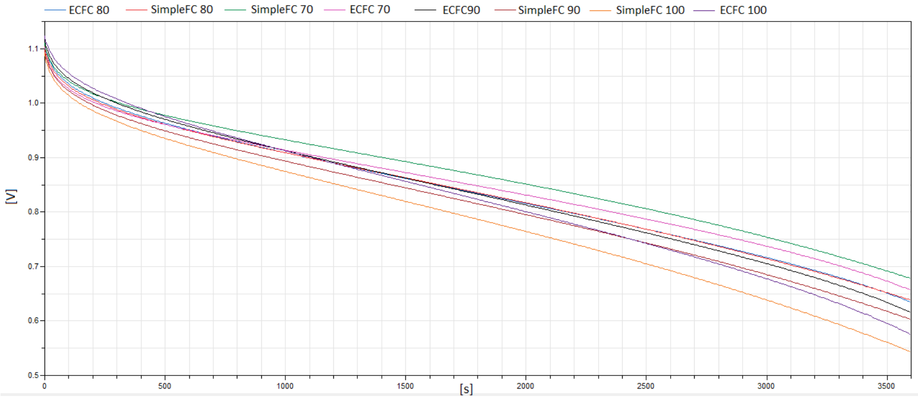

Figure 4.1 Comparison of the membranes in the temperature interval 70-100°C.

Nevertheless, the voltage also slightly increased with increasing reactant pressures and was also improved when the relative humidity in the anode or the cathode was increased, as shown in Figure 4.2 and 4.3. These observations are discussed in Chapter 5.

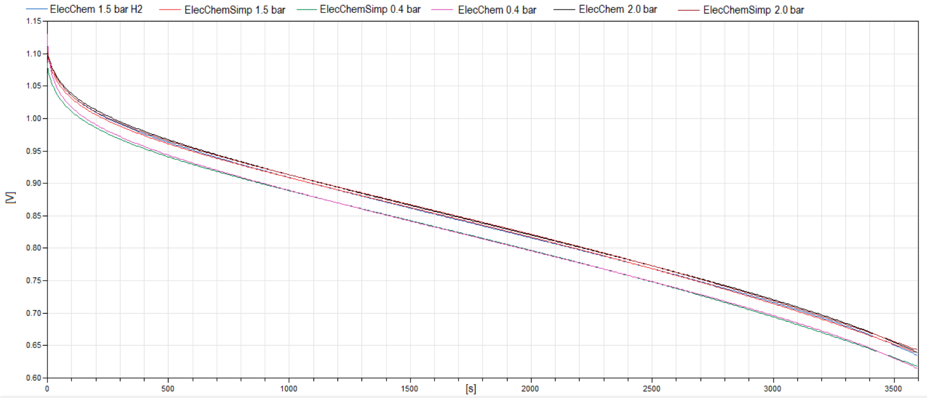

Figure 4.2 Comparison of the membranes in the H_2 pressure interval 0.4-2.0 bar.

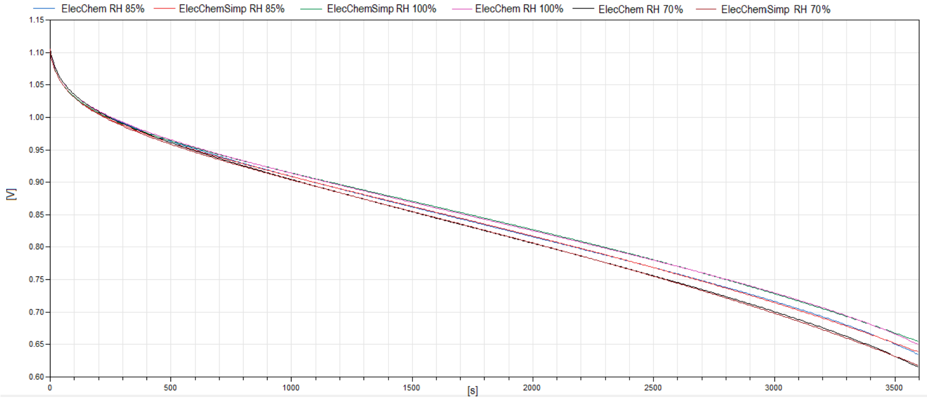

Figure 4.3 Comparison of the membranes with the relative humidity of the air varied between 70-100% RH.

Water Transport Membrane

The different mass flows and enthalpies were verified by hand calculations and found to coincide. However, when run in the membrane test and in the stack test, the net water was found to flow from the cathode to the anode, and not as expected, the inverse.

During the stack testing, it was also discovered that the hydrogen at the anode side was able to carry unrealistically large amounts of vapor, without becoming saturated. This was not further attended, but could possibly result from an implementation error in the medium model.

Due to the unresolved errors in the *Water Transport* membrane, this membrane was never validated. Instead, in the rest of the project, the *Electro Chem* membrane was used during the development.

4.3 Fuel Cell Stack

For the three water management options of the component, the mass flows and energies were verified to agree with expectations. During the validation, the different optional models were further evaluated.

The separator option was identical to its reference component, the *Condensing Volume*, while the condensing option only showed a similar behavior as its reference component, the *Distributed Channel Moist Air* component.

Since the condensing volume and the separator model were built on the same structures and the equations were the same, the component behavior was identical.

The condensing model, where equations from the *Distributed Channel Moist Air* component were implemented in the *Condensing Volume* template, gave a similar, but not identical behavior. Compared to the separator option, the condensation option resulted in a slightly higher component temperature.

Some of the variables for the separator option and the condensation options are showed in Figure 4.4 and 4.5.

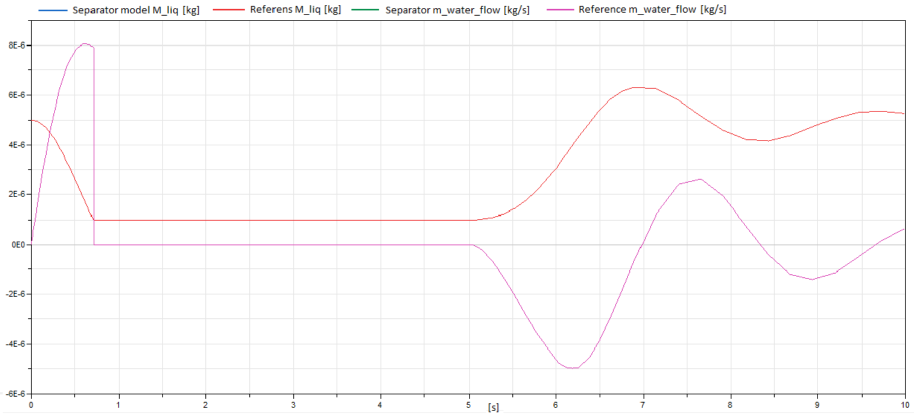

Figure 4.4 The separator model versus the reference condensing volume model. The variables M_{liq} and $m_{water,flow}$ are exactly equal in both models.

For the condensation option of the component, the equations declaring the physical behavior are equal to the ones in its reference component. However, the structures of the reference component and the option implemented have several differences. In the reference component, the water will leave the component immediately when condensing. In the condensation option, water will physically stay in the com-

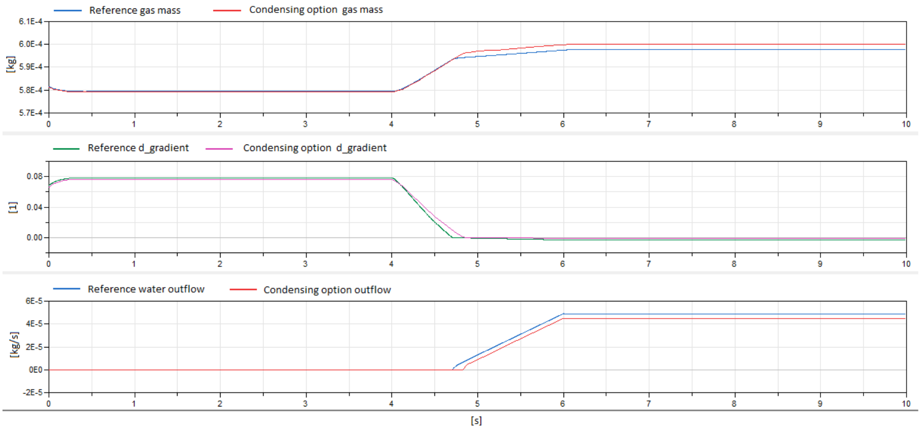

Figure 4.5 The condensation model versus the reference distributed pipe channel model. The different variables follow each other fairly well.

ponent and then be able to affect certain properties, although still being unreachable for the rest of the system.

The third choice of the model, where the condensation was shut off, was also checked to verify that no unexpected mass or energy exchange occurred. Thereby, this option behaved as expected.

This model still allows liquid water carried by the gas flow (i.e. $X_{liq} > 0$), but no liquid water condensed and drained in the channel volume (i.e. $M_{liq} = 0$).

The different component options were also tested in a stack test. It was found that during the operation conditions intended for the stack system, no condensation would occur for any of the component options.

4.4 Stack Cooling System

The cooling system was carefully tested in the stack temperature range 55-100°C to monitor cooling temperature, water flow, heat exchanger in and out temperatures, pump speed and pressure. The hydrogen inflow temperature was also varied from 25°C and up to the stack temperature to verify if the stack temperature and cooling water temperature profiles would be effected by this, but no such effect was observed.

The PID controller was evaluated by comparing the plots of the stack temperature and the cooling temperature in the uncontrolled system with the controlled system. Figure 4.6 displays the result.

The construction of the cooling system and its control was a rather straight forward part of the work, since many components were already available. The performance of the cooling system was satisfactory.

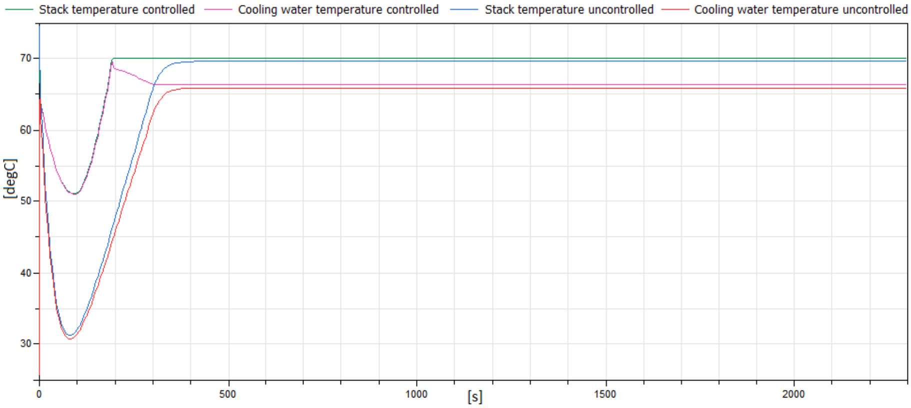

Figure 4.6 The stack and cooling temperature at stack reference temperature 70°C, before and after control implementation. (The current was ramped to 300 A during 300 s and then maintained at steady state.)

4.5 Humidifier System

When validating the *Simple Water Mix* component towards the psychrometric chart, the results were found to coincide at lower temperatures or humidities, but to deviate slightly at higher temperatures or humidities.

Potentially, this could be related to the simplification of the physical model, which would change the steady state behavior to a minor extent.

Since the chart did not allow comparisons in the temperature intervals intended for the humidifier and since over-saturated systems were not taken into regard, the component could not be fully verified. By this, it could not be stated if the model behavior at $X_{liq} > 0$ was correct, especially not when larger fractions of liquid water were injected into the system. The external warming of the mixing chamber would lower the fraction of X_{liq}, and as a bonus, thereby decrease the uncertainty of the model.

In the humidifier validation test, the amount of water brought in by the air plus the amount of water produced in the stack turned out to be insufficient to humidify the system at temperatures above 80°C, when the system was not allowed to inject more water into the humidifier than what was removed by the water separation process. This is due to that at higher temperatures, air is able to hold an essentially larger amount of water before reaching its saturation level. Consequently, then a larger amount of water will also be required to reach the desired relative humidity level of the system. This problem was however automatically resolved once the humidifier was connected to the stack system and the water amount pumped into the system was controlled according to the relative humidity level of the stack. The water pumped into the stack was recollected by the separator and filled the water tank up at any stack temperature.

The stack system with the humidifier was tested in the interval 60-100°C and was found to work as expected.

The humidifier was never implemented on the anode side of the system. According to a series of patents considered regarding humidifier systems, it seems more common to only have cathodic humidification [Toyota Motor Corp, 2007].

The manually adjusted PID controller performed reasonably during stack system simulations in the interval 60-100°C.

Adjusting the PID controller was time consuming, since the control parameters had to be reconsidered when different conditions were tested. The hardest situation to resolve, was system initialization at 60°C, as the humidity easily peaked above saturation level to flood the stack.

Worth mentioning is also that the humidity of the stack is calculated assuming that the incoming air temperature will immediately reach the stack temperature as it enters the stack.

After the implementation of the humidifier in the stack system, the system would require 1 simulated second of start-up time for humidification, prior to initializing the withdrawal of current. This implied that the current profile of the system test had to be changed.

4.6 Air and Fuel Supply

At the anode side, all flows were verified to coincide and to change in the expected directions when the anode pressure was varied. The automatic pressure regulation of the system (described in the Implementation subsection of Section 2.7) is simple and efficient and requires no external controller.

In the implemented solution, the system is controlled in order to make the rotational speed increase according to the fuel consumption, which implies that the cathode behavior is directed by the anode behavior. This is convenient, although it is a feed-forward proportional control, and not a feedback solution.

Calculations of air usage and temperature increase of the compressor were also performed and compared to literature examples [Larmine and Dicks, 2003]. According to the results, the parameter ranges seemed to be properly chosen.

4.7 Flow Machines

To display a typical result, the different power consumptions at a stack temperature of 70°C and a steady state current of 450 A (the intended max current of the system) are shown in Table 4.1.

It is difficult to determine the reasonableness of the power consumption calculations, but at least they appear to be in the correct order of magnitude. For simplicity, in the model, the power development of the pumps were implemented to increase

Device	***Power (W)***
Compressor	16 000
Cooling pump	730
Humidifier pump	2.8
Fan	13

Table 4.1 Power output of the auxiliary device of the stack. During these circumstances, the auxiliary device consumed 14% of the stack power produced.

linearly with the pressure head, but in a real system it would rather follow an exponential behavior. Due to the insecurities of the power consumption estimations, the linearizion performed should be sufficient for this model.

Since all modules of the final stack system were now completed, the system was evaluated and tested and was found to behave as desired.

In the current profile, ramps of variating steepness of their declinations were also tested to verify the model performance. A step from 0 to 450 A will interrupt the simulation, but if the current interval is ramped up during a few seconds, the simulation will run, but become very slow, due to the stiffness of the differential algebraic equations (DAEs).

4.8 Current Control Logic

The maximum power output of the stack was found to improve at lower stack temperatures, since the cell voltage increases as the temperature falls. The stack temperature for further parameterization was chosen to 70°C.

According to Equations 2.49 and 2.9, i_{max} and $\eta_{voltage}$ at I_{max} were calculated to 0.56 A/cm^2 respectively 57%, which corresponds to the cell voltage 0.71 V. The current density can be compared to available voltage-current density data points; (0.3 A/cm^2 at 0.8 V and 1.41 A/cm^2 at 0.679 V) [3M Company, 2016]. The efficiency seems reasonable, but the current density is about 2.5 times too low at 0.7 V.

The FCHV system was simulated and the stack current followed the positive part of the motor current well.

A coefficient in the filter component also had to be adjusted in order for the current signal to change slower to make the system more robust and to minimize unnecessary charging of the battery. The filter coefficient was not optimized, but gave an acceptable performance.

The final full FCHV system was tested and found to behave as experted, so as a next step, it should be validated.

4.9 Validation Results of Full FCHV System

During the validation process, flows were verified to coincide as expected and the system behavior was compared to information of fuel cell systems achieved from literature throughout the project.

Based on the validation results, the system could be described and verified. Also, one advantageous stack temperature was chosen for running the up-coming drive cycle tests.

The battery SOC is found to grow throughout the validation cycle. The battery releases energy during accelerations and is charged during deceleration. However, more energy is charged to the battery during the decelerations than what is withdrawn during the accelerations, as shown in Figure 4.7. This is due to that the current withdrawing algorithm is simple and the filter coefficient is not optimized.

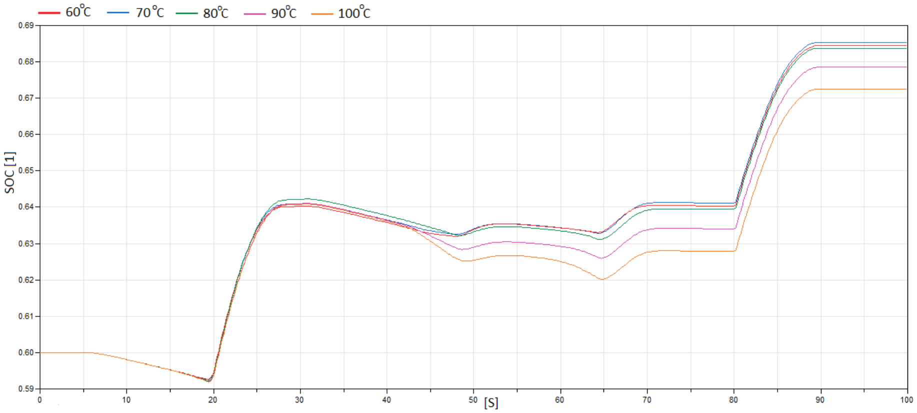

Figure 4.7 The SOC of the battery during the validation cycle.

Just as expected, the motor operates independently of the stack temperature, obtaining the same current and delivering the same torque.

The power output decreases with increasing stack temperature due to decreasing stack voltage (and cell voltage, as displayed in Figure 4.8). By this, the cell voltage efficiency will also decrease. However, the current compensates partly for the power loss by increasing slightly with falling cell voltage, and hence, so does the current density. Optimal stack efficiency is a trade-off between the operating conditions of the stack and the power consumption of the flow machines. The fuel cell is more efficient at higher pressure and lower temperature, but elevated pressure increases the load on the compressor. Since the same mass of air requires a larger volume at higher temperatures, the compressor also has to work harder and thereby increase power consumption at higher temperatures. As a result, the stack net power and thereby the power efficiency decreases with increasing temperature and pressure.

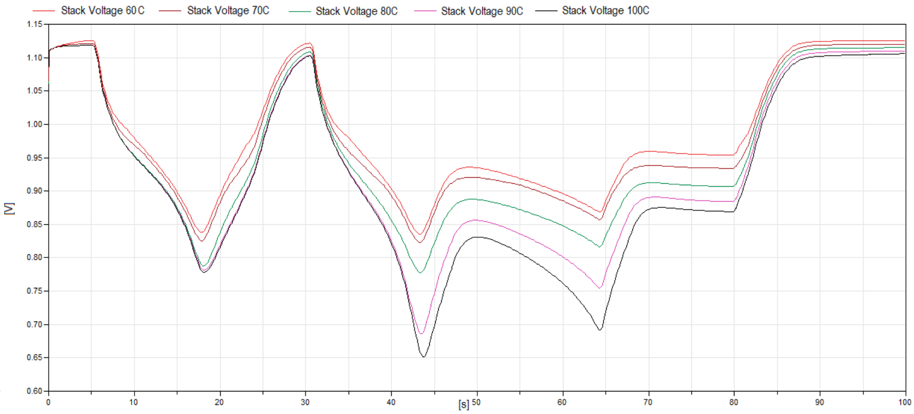

Figure 4.8 The cell voltage at different stack temperatures during the validation cycle.

In a V-I plot, the cell voltage is plotted as a function of the current density, as shown in Figure 4.9. The current density during the validation cycle is even lower than the results received in Section 4.8. The single cell voltage remains in the same range as earlier, 0.7 - 1.1 V, but the lower power demanded results in a lower current withdrawn.

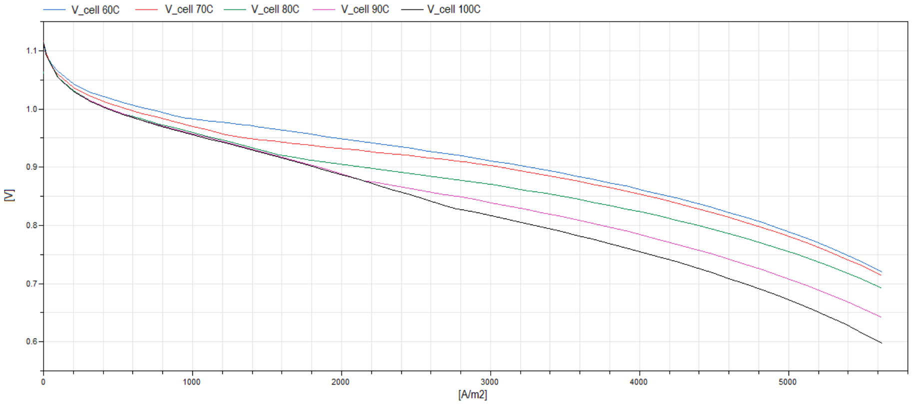

Figure 4.9 V-I-plots at different stack temperatures during the validation cycle.

The cathode pressure, illustrated in Figure 4.10, and the cathode volumetric flow varies with temperature and compressor speed. Higher pressure and flow are obtained at higher temperature. The cathode pressure has to be increased to compensate for the decreasing cathode stoichiometry. The anode and cathode stoichiometry decreases with increasing temperature, since efficiency then decreases. This is due to that more reactants are consumed at higher temperatures, but for less power produced. With the present compressor settings, the cathode stoichiometry at the higher stack temperatures will still be marginally too low.

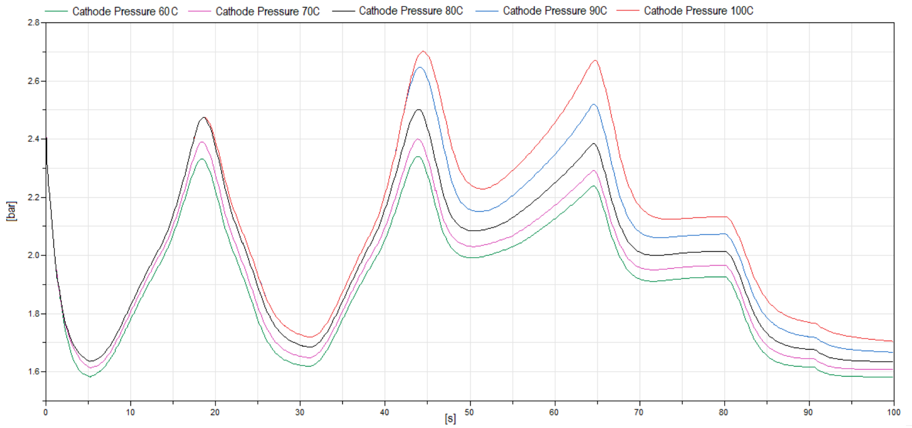

Figure 4.10 The cathode pressure variations during the validation cycle.

An important, but sensitive process is to control the relative humidity in the stack. This is illustrated in Figure 4.11. The most stable behavior is found at 70°C. Although the humidifier PID is carefully adjusted, some fluctuations remain at 60°C during start-up, especially when the humidifier warming function is disabled. At higher temperatures, the signal also becomes less stable. The large dip at 100°C is however caused by the limitations in humidifier water pump flow, whose capacity was found to be slightly inadequate at 100°C. However, this is not essential, since the system is not designed for and PEM fuel cells are generally not operated at temperatures this high.

When the fraction of liquid water in the humidifier air, X_{liq}, was evaluated, there was found to be less liquid water in the water heated humidifier, due to the higher temperature, which increases the saturation level of water.

The behavior of X_{liq} in the humidifier is shown in Figure 4.12. At higher stack temperature set-points, the initial temperature of the humidifier is set higher than the stack temperature during start-up, before the stack temperature stabilizes. For that reason X_{liq} of the humidifier is smaller at these temperatures at the beginning of the simulation. However, at higher set-point stack temperatures, X_{liq} increases heavily later in the simulation due to the temperature difference between the humidifier and the stack.

Since a larger amount of vapor is resolved in the humidifier when the temperature of the humidifier is controlled, an obvious conclusion is that the heating func-

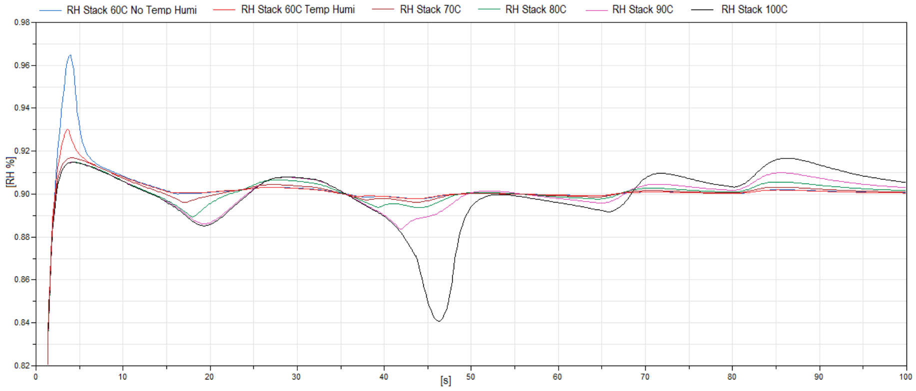

Figure 4.11 The RH of the stack. The red and the blue lines show the behavior at 60°C when the temperature of the humidifier is controlled and uncontrolled.

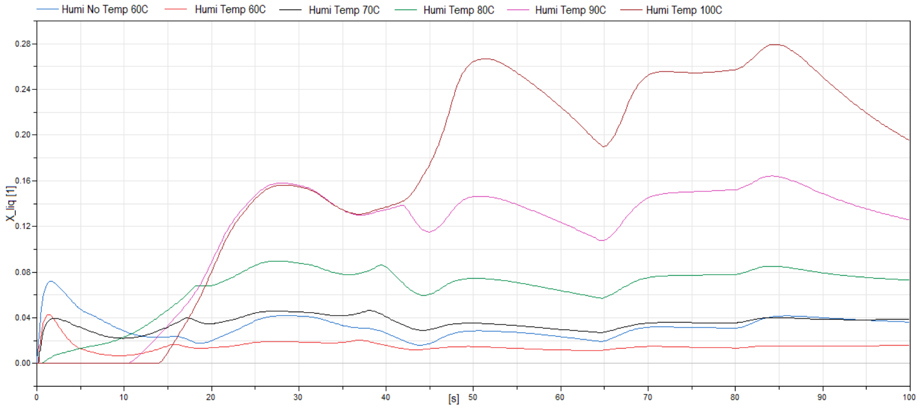

Figure 4.12 X_{liq} in the humidifier. The red and the blue lines display the behavior at 60°C when the temperature of the humidifier is controlled respectively uncontrolled.

tion of the humidifier improves the system performance and should therefore be enabled.

One of the assumptions in the stack modeling is that the gas entering the stack is always at thermodynamic equilibrium. In the stack, the gas will rapidly be heated to the surrounding stack temperature. By this, all X_{liq} will turn into vapor almost instantaneously. In real life however, it is probably not recommended to operate at the higher stack temperatures (90-100°C), in order not to risk flooding the entrance of the cathode flow channel of the stack.

The saturation partial pressure of vapor in air, i.e. the ability of the air to hold vapor, increases with temperature. For that reason, at a fixed RH set-point, there will be more water in the stack system at higher temperatures, and thereby, more water will also be retrieved in the separator at higher temperatures.

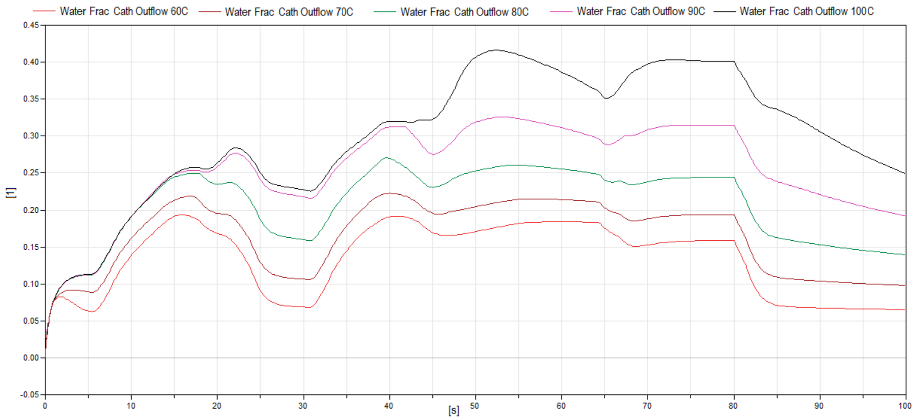

Figure 4.13 The cathode water fraction at the stack drain during the validation cycle.

In the stack channels, the water content at the cathode drain also increases with temperature, as displayed in Figure 4.13. In the anode, about 1% vapor is found in the loop. This is due to a numerical initialization calculation also found in the simple stack system. This water remains in the loop throughout the rest of the simulation, but does not affect performance. Apart from that, there is no water entering the anode and in the anode channel, there is no X_{liq} ever. In the cathode drain, condensation will only occur and X_{liq} will only be present when the car is moving.

As illustrated in Figure 4.14, the stack temperature is always higher than or almost equal to the cooling water temperature. However, it takes time for the system to warm up to reach above 90°C during driving. In the heat exchanger, the outgoing air has a higher temperature than the outgoing water. This might be surprising, since the incoming water is a lot warmer than the incoming air, but can be explained by the counter flow configuration of the heat exchanger.

Generally, the cooling system has to work harder at lower stack set-point temperatures. Cooling the stack to 60°C strains the system substantially, while at a set-point temperature of 100 °C, cooling is barely used, as shown in Figure 4.15.

The overall conclusions from the validation, is that the stack temperature should be set to around 70 °C for the future drive cycle tests. The system is not designed for temperatures above 90°C (and in real life, PEM fuel cells are almost never run at temperatures this high either). Nevertheless, the cooling system is not optimized to keep the stack temperature as low as 60°C.

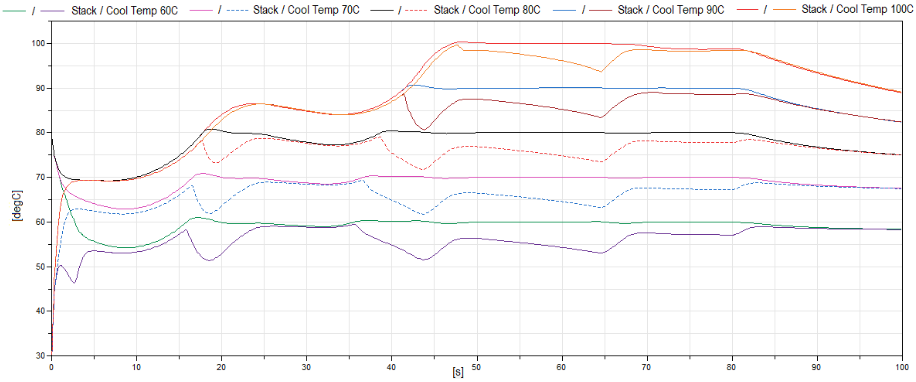

Figure 4.14 The stack and cooling temperatures during the validation cycle.

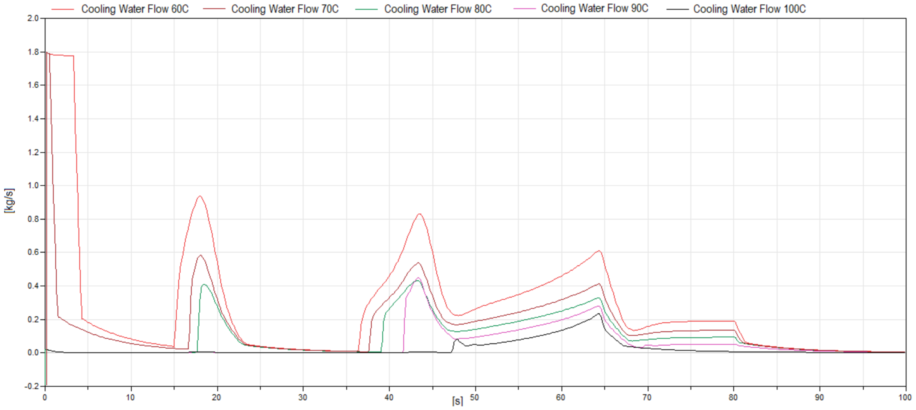

Figure 4.15 The cooling water flow at different stack temperatures during the validation cycle.

4.10 Drive Cycle Test Results

For the highway cycle, US06 HWY, the stack temperature is rather well maintained during the simulation, especially at higher ambient temperatures, as illustrated in Figure 4.16. However, in the other drive cycles, shown in Figure 4.17 and 4.18, where more frequent stops are made and the velocities are lower, the stack is unable to produce enough heat to keep the desired stack temperature. This effect is especially prominent in the urban drive cycle and at low ambient temperature. This is an unexpected deviation and will be subject to further discussion in Chapter 5.

The cooling water temperature will also decrease when the stack temperature is lowered. Actually, both for the city drive cycle, UDDS, and the mixed cycle, IM240,

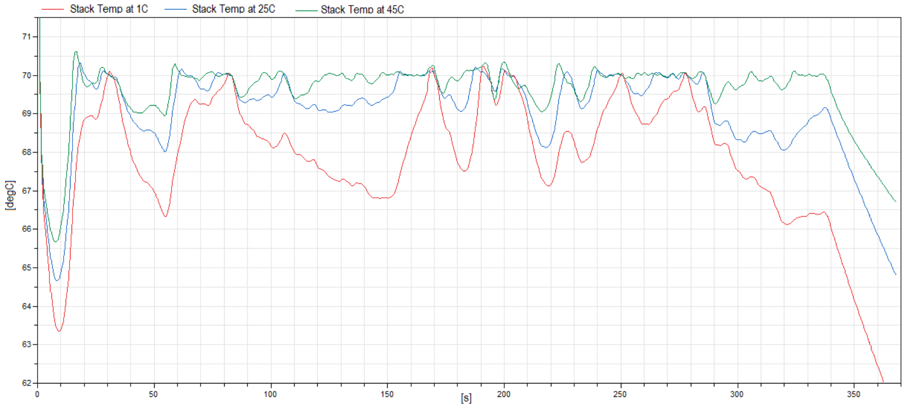

Figure 4.16 The stack temperature at different ambient temperatures during the US06 HWY cycle.

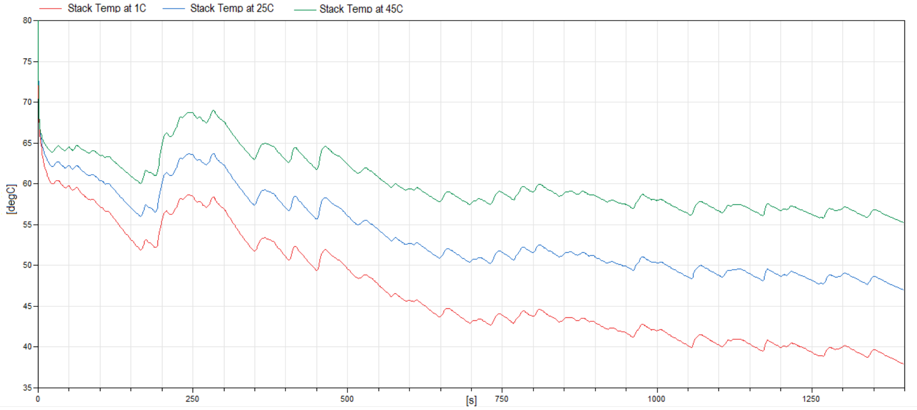

Figure 4.17 The stack temperature at different ambient temperatures during the UDDS cycle.

the cooling system is more or less turned off, due to the low stack temperature. As a consequence of this, the humidifier mixer will not be warmed and its temperature will be lowered and more unpredictable.

Efficiency is higher when driving at higher velocities. This is due to an overhead power consumption, when the motor operates in idle mode. At lower velocity, a larger share of the power consumption is caused by the overhead, since less power is demanded to move the vehicle. Just like in a gasoline car, fuel consumption is increased when driving at lower velocities with frequent stops. Figure 4.19 shows the efficiency during the UDDS cycle.

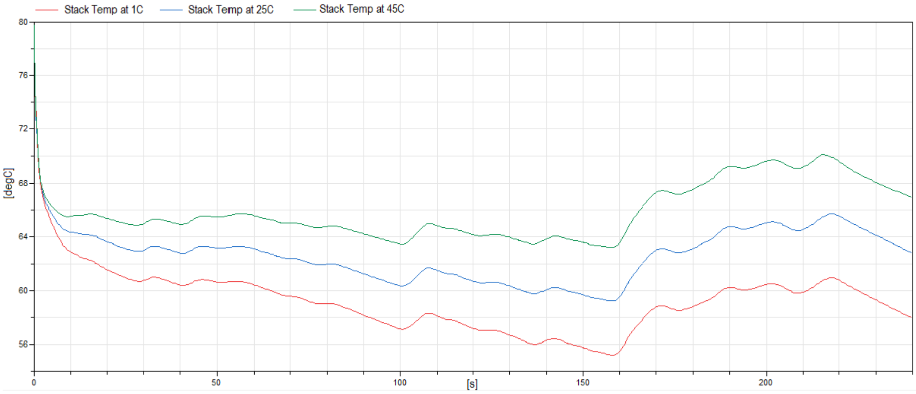

Figure 4.18 The stack temperature at different ambient temperatures during the IM240 cycle.

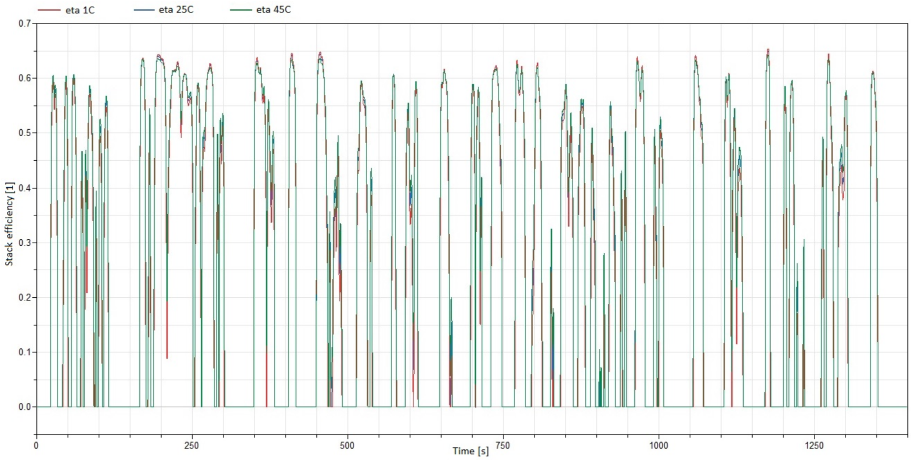

Figure 4.19 The stack efficiency at different ambient temperatures during the UDDS cycle.

The stack current is unaffected by the ambient temperature and so is the stack voltage for the highway cycle, as displayed in Figure 4.20. However, for the other two cycles, an increase in voltage is observed at lower ambient temperatures. Figure 4.21 shows the cell voltage variation during the UDDS cycle. A temperature dependence of the surroundings is not expected in the membrane, since all equations involving the ambient temperature have been exchanged for constant values. However, due to the inability of the stack control and the system design to maintain the desired temperature during these cycles, the stack temperature will drop, as dis-

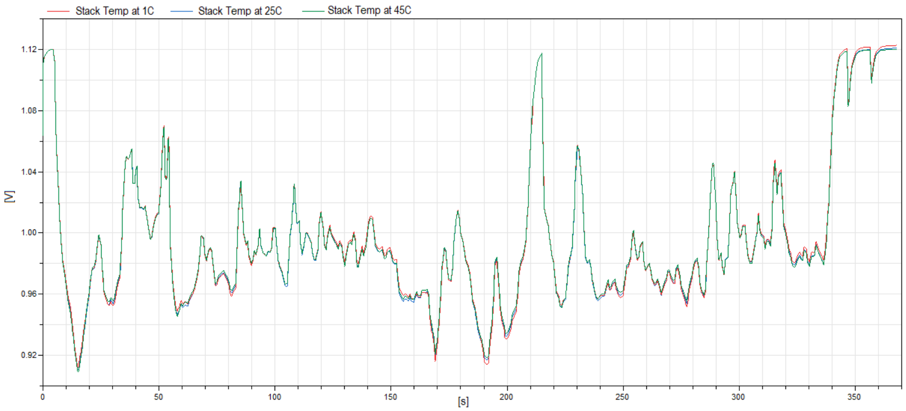

Figure 4.20 The single cell voltage during the US06 HWY cycle.

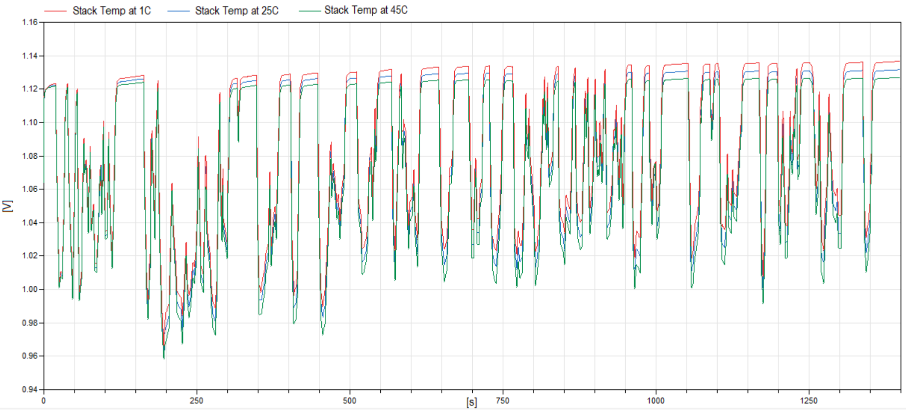

Figure 4.21 The single cell voltage at different ambient temperatures during the UDDS cycle.

cussed earlier. According to the Nernst equation, Equation 1.1, and the decreased losses, the voltage will thereby increase.

Further, when discussing current and voltage; as the voltage is plotted as a function of the current density, the current density of Figure 4.22 becomes even lower than calculated in the FCHV system chapter, Section 2.9. However, the cell voltage does not decrease much either, due to the limited power demand.

For the highway cycle, the relative humidity of the stack is slightly more unstable at low ambient temperatures, probably due to the slightly unstable stack temperature. However, for the other cycles, the relative humidity is more stable at the lower surrounding temperatures. An educated guess is that when stack temperatures

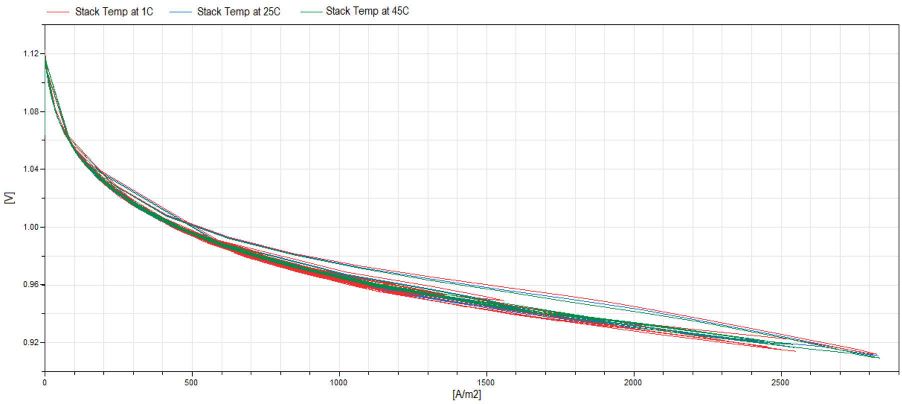

Figure 4.22 V-I-plot at different ambient temperatures for the US06 HWY cycle.

fall this low, there will be a lower demand of humidity in the system that is easier to supply in a smooth way.

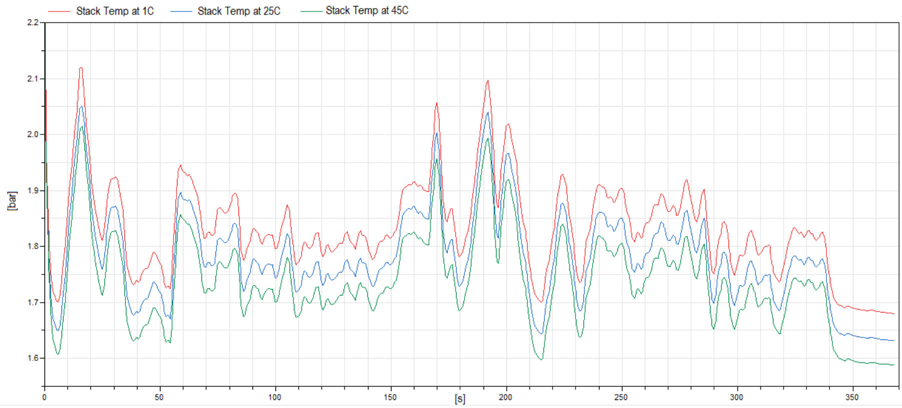

Figure 4.23 The cathode pressure for the US06 HWY cycle.

The cathode pressure was found to decrease with ambient temperature in all drive cycles. Figure 4.23 illustrates the pressure fluctuations during the US06HWY cycle. This can be explained by the density change of the air at different temperatures and that the compressor works by volume and not mass pumped in. When the incoming air is warm, fewer air molecules will be pumped in per volume unit. A smaller number of molecules in the volume decreases the cathode pressure and the inverse.

5

Discussion and Conclusions

Simple Stack System

On the anodic side of the stack system, it was found that if a minor fraction of vapor or any other gas was added to the gas composition, this gas would eventually fill up the hydrogen loop. This would imply that the hydrogen partial pressure would become too low to continue the simulation. In case the hydrogen was humidified, this also caused flooding of the loop. For the simple model, where no external humidification was implemented, this bug was hidden.

Electro Chem Simple Membrane

The model seems to follow fuel cell theory - the standard cell potential, E_0, for certain increases with temperature, but the total output voltage of the Nernst equation (Equation 1.1) E, decreases [Larmine and Dicks, 2003]. Added to this are the losses, which also increase with temperature (see Equations 1.3-1.5). As mentioned in the fuel cell theory chapter, PEM fuel cells are also appropriate for operation at low temperatures.

The improved voltage output at higher reactant pressures follows from the Nernst equation. Increased relative humidity in the membrane raises conductivity and thereby lowers the ohmic loss.

The overall conclusion is that the new membrane model and the more detailed reference membrane coincide well, although there is a certain deviation between the models when the operation temperature is changed from 80°C, which is the temperature for which the new membrane was initially developed. This can be explained by that the parts of the *Electro Chem* model that have been replaced by constant values in the thesis model are temperature dependent in the reference membrane.

Water Transport Membrane

When evaluating the water transport membrane, the net water was found to flow from the cathode to the anode. This depended on that the electro-osmotic drag (proportional to the current) from the anode to the cathode was a lot smaller than the back-diffusion in the opposite direction (which is proportional to the water concentration gradient across the membrane). In a real stack system, there is no water flow from the membrane into the anode and all water is supposed to exit through the cathode.

Since the water concentration at the anode was always significantly lower than the water concentration at the cathode, where water was formed, this could be one of the explanations why the water flow got this undesired direction. This was particularly prominent at higher stack temperatures, when the absolute water amount at the cathode is larger, thereby enhancing the concentration gradient. However, it was possible to reach certain operation points at lower temperatures combined with a high current withdrawn from the cell, where both the anode side and the cathode side were humidified. Here, the flow went in the correct direction, but it would not be possible to run the system under these conditions in the real system.

This was investigated further and it was believed that the energy equations were not properly implemented, either in the membrane or in the medium model.

Initially, when constructing the water transport membrane and the new channel component, the intention was that vapor in the anodic and cathodic reactants should be able to enter the membrane. For that reason, the anodic port of the membrane was modified to allow water transport. When the water flow through the membrane was firstly going in the wrong direction and secondly, all too large, it was anticipated that something was wrong with the energy generation equations and also with the set-up of the stack test. It was also believed that the water management would resolve once these issues were dealt with. However, the criteria of no water removed from the anodic side, should have been hard coded. If the membrane is remodeled so that no water can exit through the anode, it might also be necessary to set a max volume for the amount of water allowed in the membrane component.

Channel Component of the Stack

To summarize the channel component, the separator model is always at equilibrium and removes water according to a time constant, where the user can decide how fast water is to be collected. In contrast, the condensing model is not at equilibrium and is driven by a temperature gradient between the component wall and the gas.

However, as more understanding for the system was developed, it turned out that the condensing model was not applicable for the conditions necessary for the stack to operate realistically for two reasons.

Firstly, the stack system is implemented according to the assumption that the gas in the stack is immediately heated to the same temperature as the component wall. This rules out the essential condition for condensation.

Secondly, in the model, condensing water is assumed to leave the component immediately in an irreversible process when stored in the unreachable variable M_{liq}. In reality, condensed water can stay in the stack, potentially blocking the channels and the fuel cell active area. For that reason, a complimentary vaporization model is required to remove the water in order to work as intended.

Information and equations describing the evaporation was not available and due to time limitations, the model was not further developed.

Since the condensation part of the component was not applicable to the stack system, the rest of the thesis work was performed either by using the original *Condensing Volume* component or the new channel component in the separator option.

Air and Fuel Supply

In the Implementation subsection of Section 2.7, different ways of controlling the hydrogen flow on the anode side were discussed. Concerning the idea of using the cathode stoichiometry as a measurement signal, it was found to operate in a large range and could vary from 0-100. 100 is the upper limit reached when the stack system is idle and during high power generation, it falls to around 2. Hence the reference signal for this measurement signal would also have to vary with the degree of power withdrawn from the stack. This would be difficult to implement and for that reason, the cathode stoichiometry should not be used as a measurement signal.

As mentioned earlier, the cathode pressure is a trade-off between compressor power consumption and the oxygen partial pressure. The cathode pressure of the system was found only to have a very limited effect on the cell voltage. However, the power consumption, which was just a rough, probably under-dimensioned estimation, increased significantly when the pressure was increased. For those reasons, a cathode stoichiometry slightly below 2 seemed sufficient (as mentioned earlier, 2 is a typical value of the cathode stoichiometry [Larmine and Dicks, 2003]).

After implementing the compressor control system, a suggestion found in literature [Pukrushpan, 2003] was to control the compressor either as a function of the current withdrawn from the stack or as a function of the oxygen partial pressure at the cathode outflow. The implemented system is rather closely related to controlling the compressor according to the current. Anyhow, it also compensates for that the stack efficiency falls at higher currents, after reaching its maximum, due to the decreasing cell voltage (remember the profile of the V-I plot). This implies that fuel consumption increases faster than the current. Thereby, the implemented solution over-predicts the required consumption of air and signals to the compressor to work harder than if the process was controlled by the current.

Possibly, it is more advisable not to increase the power consumption of the compressor too much, when the efficiency of the cell is already decreasing.

Power Tables

Since no information about power consumptions of pumps or fans was available, it was hard to know if the tables were in the correct power range. The compressor power is however known to dominate completely also in a real stack system [Kim and Peng, 2007]. A literature example of a compressor of about the same dimensions as the developed system, but using the compression ratio of 3 instead of 2.5, as in the thesis, has a power consumption of about 20 kW [Larmine and Dicks, 2003]. According to other sources, the compressor can consume up to 30% of the stack power generated [Kim and Peng, 2007].

The power tables can preferably be changed in the future, when the model is adapted to a real system.

Current Density

Compared to available voltage-current density data, the current density should be higher than the one obtained. This can partly, but not fully, be explained by the large cell area (most cell area data encountered in literature during the project was found to be smaller, but the intended application areas of these fuel cells are unknown).

During the parameterization, the cell area had to be increased about 8% compared to the calculated cell area. Partly, this was due to the extra margin taken into regard for losses in the water transport membrane. The rest can be explained by that the stack temperature is not optimized and of error margins in the cell voltage.

The cell voltage losses have not been fitted according to the Mirai system, since the power characteristics were not available. Thereby, the parameters describing the losses are not representative for the Mirai.

According to the model, the optimal stack temperature would be found below the applied 70°C. If it is lowered, the maximum effect will increase. Then the cell area can be decreased and the current density will raise.

Current Directing Algorithm

The current directing algorithm used in the model is very simple, but could preferably be exchanged in the future. The algorithm limits performance, since the battery can be charged to 100% and will thereafter just lose the extra energy produced. For that reason, the algorithm and the filter have to balance the SOC of the battery better.

Drive Cycle Tests

A general conclusion from the drive cycle tests are that the model performs well during highway driving and at higher speeds with no frequent stops. However, due to the temperature drop in the stack, the model does not behave as good for irregular drive cycles or at lower velocities as in the city or country road drive cycles. On the other hand, the problems of maintaining the stack temperature actually mirror behaviors also to some extent occurring in reality.

During these drive cycles, it also turned out that the stack was not even close to using its maximum power level and this is how the system is designed to operate. This, by itself, is not a problem, but at such limited power development, the stack gets difficulties keeping its assigned temperature, particularly during city driving with frequent stops. In a real vehicle, several heat producing devices, such as compressor and AC system are enclosed in a limited space together with the stack. These devices will develop heat both while the vehicle is moving and when standing idle. Heat transfer between these components has not been considered in this model and that could possibly contribute to the temperature drop observed.

However, a first task would be to review the stack parameterization, since in this work, the heat capacity values from the available components have been used by default. Values should be searched for in literature or an estimation of their correctness should be performed. For example, during the UDDS cycle at the ambient temperature of 25°C and with the cooling system turned off, the stack temperature drops from 64°C to 57.5°C during 70 s (see Figure 4.17). This occurs in a stack device having a volume of 37 L and a mass mainly constituting of metal, composites and cooling water, still during a minor heat development. Spontaneously, this temperature decrease appears to occur a bit too fast.

Concerning simulating drive cycles in a future model containing a completed *Water Transport* membrane, this could be troublesome, since the drive cycles tend to operate at lower power outputs. The electro-osmotic force driving the water flow through the membrane in the desired direction from anode to cathode is proportional to the stack current and may be insufficient at lower currents. (Recall Equation 2.10.)

General Discussion and Conclusions

The final FCHV system model is believed to be rather similar to Toyota Mirai, apart from that the model has an external humidifier and a DC motor instead of an AC motor. However, as earlier discussed in Section 2.2, the DC motor model is actually a way to get a both simpler and more accurate motor model.

Modeling the hydrogen tanks has also been omitted, since this was not a central part of the model. For that reason, the hydrogen supply was simply implemented as an ideal source. Moreover, several other details of the Mirai system were not published and had to be estimated.

A general conclusion observed is that the lower the stack temperature, the better the performance. However, in a real stack, the water management will be a limiting factor at lower temperatures, since condensation will increase in the channels and maybe even occur in the membrane. For that reason, it will be necessary to implement the water transport membrane and to extend the channel component model. The water management system must contain functions to measure when the water starts affecting the system negatively.

At lower temperatures, the compressor power consumption is decreased, but inversely, the cooling system is more strained and must be dimensioned for its appropriate operation range.

To summarize, the final model fulfills its purpose, stated in Section 1.1, that is to be able to monitor overall performance and efficiency satisfactory. The answer of the question formulation of to what extent the model produces a realistic system behavior, would be that it meets its expectations, although there will always be room for improvements. The system is parameterized according to available Mirai system information, different operation conditions can be evaluated and important processes are monitored during simulation. The system works above 0°C and passed validation well. However, the stack temperature drop during some drive cycles causes problems. Hopefully this can be resolved by changing the heat capacity of the stack, if this turns out to be in accordance with the performance of a real system.

Once the stack parameters have been adjusted, it will likely be appropriate to lower the stack temperature to about 65°C to improve performance of the model. Lowering the temperature below 70°C is reasonable and remains within the most common stack temperature range of a PEM fuel cell, 60-80°C [Yoshida, T. and Kojima, K., 2015].

There are several ideas of how to improve the model in the future, and suggestions are provided in the next chapter.

6

Future Work

As a suggestion for further development of the fuel cell hybrid vehicle system model, the following proposals should be considered. The two uppermost have the highest priority.

- Look over the stack and membrane parameterization, since this might resolve or at least limit the drop in stack temperature during city driving. In other cases, implement heat transfer from the surrounding auxiliary equipment.
- Resolve the issues of the water transport membrane model. For a complete picture of the important water management of the stack system, the channel component created in this thesis should also be extended to model the accumulation and draining of liquid water in the flow channels. The most correct way to do this, would be to implement a cross-flow discretized stack model to study the spatial non-uniformity in the fuel cell stack. The non-uniformity is an important part, that has been omitted in this project.
- Implement high pressure hydrogen supply tanks and pressure reduction valves, successively transforming the hydrogen down to lower pressures. For the high pressures, implement a real gas model for hydrogen.
- Implement a membrane humidifier which is more widely used. If information of the underlying physics can be acquired, substitute the external humidifier for an internal one, since this is an emerging trend within fuel cell technology.
- Extend the current hydrogen circulation loop with an ejector component model. Since the pressure in the loop should be able to vary between 0.4-2.0 bar as a part of the control [Toyota, 2016b], another kind of control solution should also be used for the loop.
- In the present cathodic control solution, the compressor rotation speed is determined from the hydrogen consumption at the anode in an open loop structure. To obtain a feedback control system, the compressor speed could instead

be controlled from the oxygen pressure at the cathode outlet. This opportunity, as well as the possibility of controlling the compressor as a function of the current drawn from the stack, is also proposed in literature [Pukrushpan, 2003].

- For a more complete model of the cooling system, it could be extended by a radiator fan with an efficiency table, controlled by the temperature of the cooling water.
- The electric power train of the system could also be complemented by a controlled cooling system with power consumption tables. At this point, a function for calculating the full vehicle efficiency could also be implemented.
- A system for transferring electricity from the battery to the auxiliary devices of the stack system and the power train would make the full system model even more advanced.

7

Appendixes

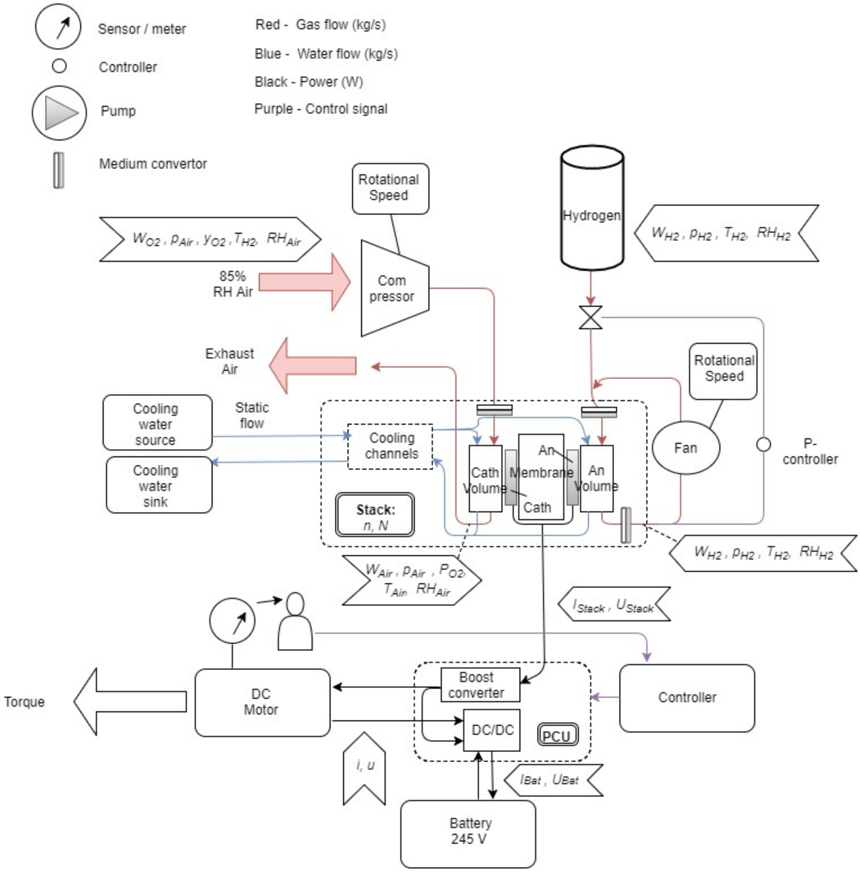

Figure 7.1 Structural overview of the Simple System.

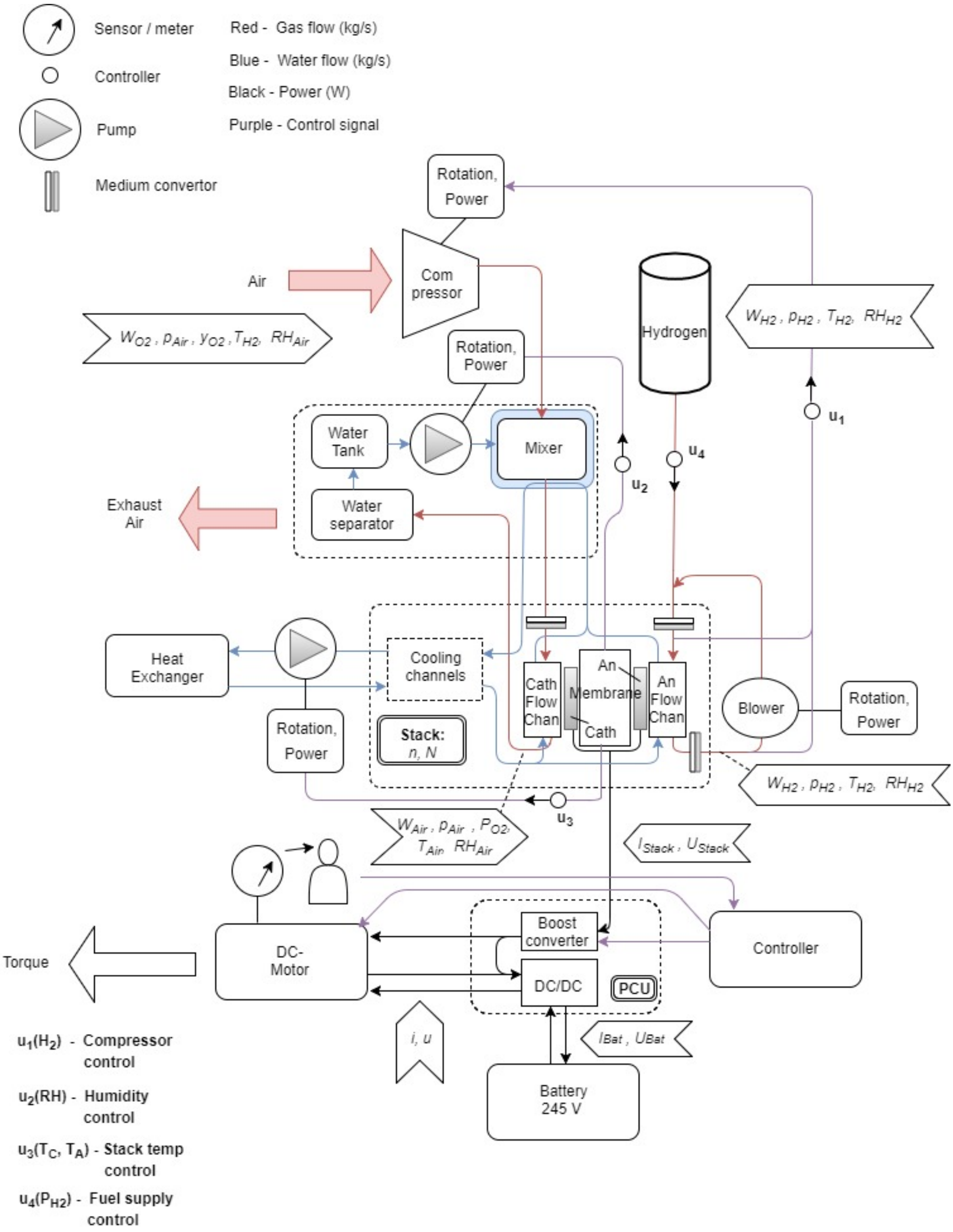

Figure 7.2 Structural overview of the Final System.

Bibliography

3M Company (2016). *High Performance, Durable, Low Cost Membrane Electrode Assemblies for Transportation Applications*. Technical Report DE-EE0005667. 3M Company.

Amphlett, J., R. Baumert, R. Mann, B. Peppley, P. Roberge, and T. Harris (1995). "Performance modeling of the Ballard Mark IV solid polymer electrolyte fuel cell". *Journal of Electrochemical Society* **142**:1, pp. 1–8.

Björk, M. and R. Levenhammar (2017). *Relay Auto-tuners in Modelica*. MA thesis. Faculty of engineering, LTH, Lund University.

Chan, C., A. Bouscayrol, and K. Chen (2010). "Electric, hybrid, and fuel-cell vehicles: architectures and modeling". *IEEE Transactions on Vehicular Technology* **59**:2, pp. 589–598.

Chen, D. and H. Peng (2005). "A thermodynamic model of membrane humidifiers for PEM fuel cell humidification control". *Journal of dynamic systems, measurement and control* 127, pp. 424–432.

Chen, D., W. Li, and H. Peng (2008). "An experimental study and model validation of a membrane humidifier for PEM fuel cell humidification control". *Journal of power sources* 180, pp. 461–467.

Cipollone, R., D. Di Battista, M. Marchionni, and C. Villante (2015). "Model based design and optimization of a fuel cell electric vehicle". *Energy Procedia* 45, pp. 71–80.

Cunningham, W. (2014). *Toyota Mirai: The 300-mile zero-emission vehicle*. `https://www.cnet.com/roadshow/auto/2016-toyota-mirai/preview/`. (Visited on 10/15/2017).

Dassault Systèmes (2017). *Catia systems engineering - Dymola*. `https://www.3ds.com/products-services/catia/products/dymola/key-advantages/`. (Visited on 10/17/2017).

Dieselnet (2017). *Inspection & Maintenance Driving Cycle IM240*. `https://www.dieselnet.com/standards/cycles/im240.php`. (Visited on 01/04/2018).

Dunlop, S. (2008). *A Dictionary of Weather*. Oxford University Press.

Dutta, S., S. Shimpalee, and J. Van Zee (2001). “Numerical prediction of mass-exchange between cathode and anode channels in a PEM fuel cell”. *International Journal of Heat and Mass Transfer* 44, pp. 2029–2042.

Emobility (2017). *Elbilens andra fördelar*. `http://emobility.se/startsida/elfordon/elbilens-andra-fordelar/`. (Visited on 08/23/2017).

Energizer (2010). *Nickel Metal Hydride (NiMH) Handbook and Application Manual*. `http://data.energizer.com/pdfs/nickelmetalhydride_appman.pdf`. (Visited on 10/11/2017).

EPA (2017). *Dynamometer Drive Schedules*. `https://www.epa.gov/vehicle-and-fuel-emissions-testing/dynamometer-drive-schedules`. (Visited on 02/10/2018).

Eric Durling (2017). *Modelon Gothenburg*. Personal communication. (Visited on 10/09/2017).

Gröger, O., H. A. Gasteiger, and J. Suchsland (2015). “Review - Electromobility: Batteries or fuel cells?” *Journal of The Electrochemical Society* **162**:14, A2605–A2622.

Jung, S. H., S. L. Kim, M. S. Kim, Y. Park, and T. W. Lim (2007). “Experimental study of gas humidification with injectors for automotive PEM fuel cell systems”. *Journal of power sources* 170, 324–333.

Kabza. A (2016). *Just another fuel cell formulary*. `http://pemfc.de/FCF_A4.pdf`. (Visited on 08/31/2017).

Kim, J., S.-M. Lee, S. Srinivasan, and C. E. Chamberlin (1995). “Modeling of proton exchange membrane fuel cell performance with an empirical equation”. *Journal of Electrochemical Society* **142**:8, pp. 2670–2674.

Kim, M. J. and H. Peng (2007). “Power management and design optimization of fuel cell/battery hybrid vehicles”. *Journal of Power Sources* **165**:2, pp. 819–832.

Kristensson, J. (2017a). “Biljätten: framtiden är vätgasdriven”. *Ny Teknik* 25, pp. 14–15.

Kristensson, J. (2017b). “Den stora omställningen har börjat”. *Ny Teknik* 41, pp. 4–5.

Kroos, K. A. (2016). *Thermodynamics for engineers: Physics, Thermodynamics*. Cram101 Textbook Reviews.

Larmine, J. and A. Dicks (2003). *Fuel Cell Systems Explained*. Wiley.

Modelica Association (2017). *Modelica and modelica association*. `https://www.modelica.org/`. (Visited on 10/17/2017).

Nonobe, Y. (2017). “Development of the fuel cell vehicle Mirai”. *IEEE Transactions on Electrical and Electronic Engineering* **12**, pp. 5–9.

Pihl, J. (2014). *Batteries for Selected Hybrid-Electric Vehicles, Model Years 2013-2014, (Table 33. p 117)*. `https://info.ornl.gov/sites/publications/files/Pub48613.pdf`. (Visited on 10/09/2017).

Power Circle AB (2017). *Elbilsstatistik*. `https://www.elbilsstatistik.se/`. (Visited on 01/09/2018).

Pukrushpan, J. T. (2003). *Modeling and control of fuel cell systems and fuel processors*. PhD thesis. University of Michigan.

Pumpportalen (2015). *Wet-bulb temperature*. `http://www.pumpportalen.se/driveffekt/`. (Visited on 12/13/2017).

Solsona, M., C. Kunusch, and C. Ocampo-Martinez (2001). "Control-oriented model of a membrane humidifier for fuel cell applications". *Energy Conversion and Management* 137, pp. 121–129.

Spiegel, C. (2008). *PEM Fuel Cell Modeling and Simulation Using MATLAB*. Elsevier.

Springer, T., T. Zawodzinski, and S. Gottesfeld (1991). "Polymer electrolyte fuel cell model". *Journal of Electrochemical Society* **138**:8, pp. 2334–2342.

The engineering tool box (2017a). *Fans - Efficiency and Power Consumption*. `https://www.engineeringtoolbox.com/fans-efficiency-power-consumption-d_197.html`. (Visited on 12/12/2017).

The engineering tool box (2017b). *Psychrometric Chart - Barometric Pressure 29.921 inches of Mercury*. `https://www.engineeringtoolbox.com/psychrometric-chart-d_816.html`. (Visited on 02/04/2018).

The engineering tool box (2017c). *Pump Power Calculator*. `https://www.engineeringtoolbox.com/pumps-power-d_505.html`. (Visited on 12/12/2017).

The engineering toolbox (2016). *Heat value*. `https://www.engineeringtoolbox.com/gross-net-heating-value-d_824.html`. (Visited on 02/08/2018).

Thomas, S. and M. Zalbowitz (1999). *Fuel cells green power*. Los Alamos National Laboratory.

Toyota (2016a). *2016 Mirai Product Information*. `http://toyotanews.pressroom.toyota.com/releases/2016+toyota+mirai+fuel+cell+product.htm`. (Visited on 08/29/2017).

Toyota (2016b). *Toyota Mirai FCV Posters*. `https://www.scribd.com/document/338288425/Toyota-Mirai-FCV-Posters-LR-Tcm-11-564265-1`. (Visited on 09/03/2017).

Toyota (2016c). *Toyota Mirai Specifications*. `http://www.mytoyotamirai.com/toyota-mirai-specifications/`. (Visited on 12/15/2017).

Toyota Motor Corp (2007). *Humidifier and fuel cell system*. US patent US20100151337A1. (Visited on 09/30/2017).

Yoshida, T. and Kojima, K. (2015). *Toyota MIRAI Fuel Cell Vehicle and Progress Toward a Future Hydrogen Society*. `https://www.electrochem.org/dl/interface/sum/sum15/sum15_p45_49.pdf`. (Visited on 02/08/2018).

Ziegler, J. and N. B. Nichols (1942). “Optimum settings for automatic controllers”. *trans.ASME* **64**:1, 759–765.

Lund University
Department of Automatic Control
Box 118
SE-221 00 Lund Sweden

Document name
MASTER’S THESIS

Date of issue
April 2018

Document Number
TFRT-6052

Author(s)
Sara Sigfridsson

Supervisor
Håkan Runvik, Modelon
Kristian Soltesz, Dept. of Automatic Control, Lund University, Sweden
Karl-Erik Årzén, Dept. of Automatic Control, Lund University, Sweden (examiner)

Title and subtitle
Fuel Cell Hybrid Vehicle Modeling in Modelica

Abstract

Exchanging classical combustion motors in cars for more environmentally friendly solutions is a hot topic worldwide and this has currently been taken to a new dimension by the release of the first hydrogen driven vehicles on the world market.

The objective of this master thesis has been to develop a Modelica model of an automotive hydrogen fuel cell system, which should be integrated in an already existing vehicle system template and be simulated in various drive cycle tests. The work was performed in the Modelica platform Dymola by means of its Fuel Cell and Vehicle Dynamics Libraries.

The model was constructed and parameterized according to available information of the commercial hydrogen driven car, Toyota Mirai.

The purpose of the developed system model was to monitor overall performance and efficiency during various dynamic drive cycles and operating conditions. The model should reproduce realistic output signals during simulation. It should also capture the effects of changes of a wide range of operation or boundary conditions, such as internal and external temperatures, operation pressure and variations in humidity in the stack system.

The developed stack system model contained controlled systems for air and fuel supply, an external humidifier and an advanced cooling system. The power consumption of the auxiliary device and the fuel cell and stack system efficiency could also be monitored. The power train system consisted of a rechargeable battery, a DC motor, two DC/DC converters and software to direct the current withdrawn from the stack according to the motor demands. The final fuel cell vehicle system model was validated and simulated in a set of established dynamic drive cycles.

The model was mimicking the Mirai well, although certain assumptions had been performed due to limited system information or reasonable simplifications.

Keywords

Classification system and/or index terms (if any)

Supplementary bibliographical information

ISSN and key title
0280-5316

ISBN

Language
English

Number of pages
1-99

Recipient’s notes

Security classification